Detection of radioactive noble gases

by

Richard Dale Montgomery

A Thesis Submitted to the
Graduate Faculty in Partial Fulfillment of the
Requirements for the Degree of
MASTER OF SCIENCE

Major: Nuclear Engineering

Iowa State University
Ames, Iowa

1984

TABLE OF CONTENTS

LIST OF TABLES

LIST OF FIGURES

Page

I. INTRODUCTION

The Nuclear Regulatory Commission requires all commercially operated-licensed facilities to maintain effluent controls and monitoring programs. Typical effluents consist of liquids and gases released to convenient streams, if available, or through a stack. The limitations and requirements for controlling and monitoring radioactive effluents are expressed in NRC regulations [1]. It is also intended that occupational exposures to radiation be as low as is reasonably achievable. Radioactive noble gases emit alpha, beta and gamma radiation, and are therefore health hazards, both direct and inhaled. Over 97 percent of the radioactivity currently released from Department of Energy facilities consists of the noble gases and tritium. Although these releases are large in terms of curies, they consist of isotopes of low radiotoxicity [2].

Radioactive noble gases such as argon, krypton, and xenon are produced by commerical nuclear power plants, research reactors, and nuclear fuel reprocessing facilities. Other radioactive noble gases (helium, neon, and radon) are not considered in this study because they are not produced at licensed nuclear facilities. A literature search showed that argon-41, krypton-85, and xenon-133 were the major noble gases used in calibrating monitoring systems [3-23]. These gases are the longest lived isotopes of each group [24].

Argon-41 is produced by research reactors from neutron activation of argon-40 in primary coolant water and surrounding air. Ar-41 has a half-life of 1.83 hours and emits a beta with a maximum energy of 1.198 MeV and a gamma of energy 1.29 MeV, both with 99.8 percent emission

probability.

Krypton-85 is a fission gas from uranium-235 and is also a decay product of bromine-85. Krypton-85 is commonly detected at commercial nuclear facilities because of its long half-life (10.7 years). This radioactive noble gas emits a beta with a maximum energy of 0.67 MeV with 99.6 percent probability and a 0.514 MeV gamma with 0.41 percent emission probability.

Xenon-133 is a fission gas from uranium-235 and a decay product of iodine-133. Xenon-133 has a short half-life (5.2 days) and is not usually detectable at commercial nuclear facilities. This radioactive noble gas emits a beta with a maximum energy of 0.346 MeV and a gamma of energy 0.083 MeV, both with 99.3 percent emission probability.

A variety of detection systems, utilizing several monitoring methods, have received a great deal of attention [3-23]. The detectors currently used for radioactive noble gas monitoring are NaI, scintillating plastic, germanium, ionization, proportional, and GM. These detectors are used with two basic methods of monitoring radioactive noble gases, on-line (dynamic) and off-line (static). The on-line method is a one-step process to provide timely information on the concentration of gases in an effluent stream or working environment. The off-line method is a two-step process in which a gas is first concentrated, and then analyzed to determine the activity concentration. Both methods are reliable and can provide an accurate measurement. There are two on-line systems currently used to monitor radioactive noble gases. The first system monitors a sample of an effluent stream at atmospheric pressure,

with the detector immersed in the gas [3-14]. The second system consists of a large-volume activated charcoal trap, in addition to the previous system [15]. This system is not very practical, since large volumes of charcoal and liquid nitrogen are required.

An advantage of the off-line method of processing samples is that it eliminates or reduces the influence of interfering contaminants, thus providing a concentrated sample suitable for laboratory measurement. Only four of the many off-line methods can be adapted to monitor radioactive noble gases. The first uses volume compression [16-19]. The sample air is compressed to high pressure, and then analyzed in the same container. The second system involves a large container with a detector positioned at its center. Samples are obtained by drawing air through the container until it is properly purged, and then closing the inlet and outlet valves to monitor [14]. The third method employs a cryogenic process using liquid nitrogen as a coolant [20-23]. Cryogenic processing is one method of removing a radioactive noble gas from air by liquifying the gas as it comes in contact with the nitrogen. The liquified gas is then vaporized and compressed into containers for detection. The fourth method, selective absorption, entails absorbing the radioactive noble gas in liquid freon [20-23]. If large collection times are needed, off-line methods are inappropriate for monitoring low activity concentrations, as the sample activity may decay to an undetectable concentration during the collection time. The choice between on-line and off-line methods, when based upon capital costs, ease of operation, and response time clearly favors the on-line system for monitoring an effluent stream with

the detector immersed in the gas.

There is still a great deal of improvement needed in the apparatus for a continuous-flow monitoring system; therefore, the objectives of this research are:

1. To design, construct, and operate an on-line system, with a detector immersed in a stream, capable of monioring radioactive noble gas concentrations at maximum permissible concentration levels, or below, in restricted or unrestricted areas of a nuclear reactor facility.
2. To develop a method for calibrating the system to a known release of a radioactive noble gas (μCi/cc) to obtain a calibration factor in units of μCi/cc/cpm.
3. To investigate the system's efficiency, beta-gamma detection ratios, and the degree of energy discrimination.
4. To operate the monitoring system to obtain information on concentration levels of radioactive noble gases.

Theoretical models using point detectors in a cylindrical chamber and in a rectangular prism were developed so that the response of a detector in a volume-distributed gaseous radioactive source would be better understood. A finite-area plane detector was then approximated by a grid of point detectors located in the base plane of a rectangular prism. A computational analysis was used to calculate incidence rates for the finite-area plane detector for the radioactive noble gases of interest.

A 90 x 250 x 6 mm plate-type scintillation detector was selected for

use in the monitoring system based on its high beta detection efficiency. A Plexiglas light pipe was used for light transmission to a photomultiplier tube. The detector and light pipe were installed in a Plexiglas sampling chamber of dimensions 40 x 40 x 63 cm. System flow rates were calibrated with a precision wet test meter. A calibration factor of 4.0×10^{-10} μCi/cc/cpm for a known release (18.6 pCi/cc) of argon-41 was determined. The monitoring system was then used for measurements of argon-41 concentrations in the vicinity of the Iowa State University UTR-10 reactor.

II. REVIEW OF LITERATURE

There is a need to determine activity concentrations in air in the vicinity of reactors similar to the UTR-10. This requires a system capable of measuring activity concentrations at least as low as the maximum permissible concentration for unrestricted areas.

Several on-line systems for monitoring radioactive noble gases of maximum permissible concentrations, and less, have been previously reported [3-14]. The simplest technique used a GM tube monitoring a continuous flow of air in a stack as reported by Brown [3]. Brown reported a calibration factor for argon-41 of 3.4×10^{-9} μCi/cc/cpm and 11 cpm above background for a lower limit of detection (LLD) of 4.0×10^{-8} μCi/cc.

Graveson [4] developed a battery-operated portable detector array using two beta-gamma sensitive dual-window pancake GM tubes. One unit detected gamma radiation only, while the other detected beta-gamma radiation. The second unit was used as a background suppressant. A LLD achieved was 3.0×10^{-8} μCi/cc for krypton-85.

Gregory and Parnell [5] developed a multiwire multiplane proportional counter system for beta detection. An anticoincidence unit was used to reduce background rates by a factor of five to achieve a LLD of 3×10^{-9} μCi/cc for krypton-85 for a three-minute sample time at a flow rate of 10 lpm. Although their system was bulky and expensive, a less extravagant system tested to 3×10^{-8} μCi/cc for krypton-85.

Gibson and Docherty [6] applied a two-detector system employing

two 13 mm disks, each 50 mm thick, of NE 102A scintillating plastic. One detector was used to monitor gamma activity, while the other was used to monitor beta-gamma activity. Differences in the net rates were used to determine activity concentrations. LLDs achieved for their system were 8×10^{-8} μCi/cc for argon-41, 3×10^{-6} μCi/cc for krypton-85, and 4.5×10^{-6} μCi/cc for xenon-133. Due to the very small detectors used, the sensitivity of their system was very low.

Barz and Jacobi [7] devised a detector arrangement for monitoring beta-emitting fission products in reactor coolant water. Their detector consisted of an annular plastic NE 102A detector, of 5.4 mm wall thickness, drawn up on 2.8 cm diameter cylinders of acrylic of lengths 8 cm, 20 cm, and 30.5 cm. Their detector thickness corresponded to the range of 1.2 MeV beta particles in this detector material. They observed that counting rates increased rather uniformly with increasing detector lengths. But, due to reflection losses in the plastic detector, the counting rate approached a saturation value dependent upon the incident energy spectrum.

Barz, Borchardt, and Hacke [8] advanced the use of the Barz-Jacobi detector by using a detector of length 20 cm for noble gas monitoring. A second, identical detector was mounted outside their continuous-flow sampling chamber for coincidence counting. The signals of both units were processed by a digital difference unit and analyzed by a single-channel analyzer. This technique reduced background by a factor of twenty. LLDs achieved were 4.0×10^{-8} μCi/cc for argon-41, 9.3×10^{-8} μCi/cc for krypton-85, and 8.7×10^{-7} μCi/cc for xenon-133. Calibration

factors obtained were 5.0×10^{-10} μCi/cc/cpm, 1.2×10^{-9} μCi/cc/cpm, and 1.1×10^{-8} μCi/cc/cpm, for argon-41, krypton-85, and xenon-133, respectively.

The review of literature yielded no material related to plate-type detector monitoring systems. As a result, all design criteria involving the plate-type detector were based on information from annular detector systems.

III. THEORY

In this section, a theoretical foundation is established for a detector located in a volume-distributed radioactive gaseous source. This work includes two methods for determining the response of the detector. The first method is based on point-source functions using single-collision theory for a point detector in a semi-infinite cylindrical chamber. The second method is similar to the first, except that the point detector is centered on one face of a rectangular prism. The second method is also used in an iterative process in which the point detector is mapped through a grid onto a portion of one face of the rectangular prism to generate a finite-area plane detector.

A. A Point Detector in a Cylindrical Chamber

It is desirable to determine the response of a detector to beta particles when immersed in a homogeneous mixture of radioactive gas and air within a semi-infinite cylindrical chamber [6]. An equation for the differential incidence rate on the area ds for beta particles is

$$dR = (dA)(d\Omega)(f), \tag{3.1}$$

where dA is the differential activity in a volume element dV at r, $d\Omega$ is the geometric attenuation, and f is the attenuation through a gaseous medium.

Figure 3.1 shows the annular volume element dV at coordinates (r,ϑ) under a rotation of 2π radians about the axis of the duct. The concentration of the radioactive gas in dV is assumed to be homogeneous

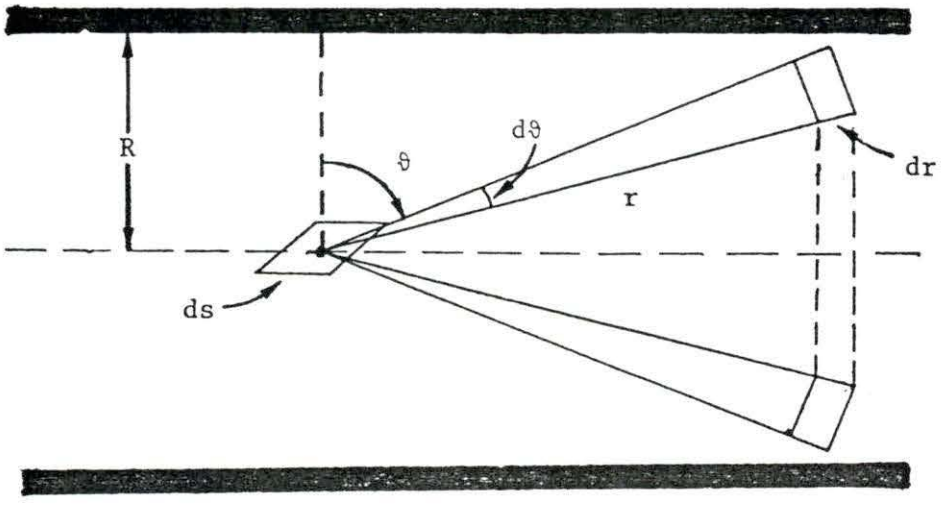

Figure 3.1. Geometry used for calculating the incidence rate for a point detector in a semi-infinite cylindrical chamber

throughout the total volume V, so that the differential activity is

$$dA = (C)(dV), \tag{3.2}$$

where C is the concentration (μCi/cc), and dV is the annular volume element ($2\pi r^2 \cos\vartheta \, dr d\vartheta$).

The probability that a beta particle in dV is traveling in the direction of ds is given by the fractional solid angle subtended by ds. This fractional solid angle is

$$d\Omega = \frac{\cos\vartheta \, ds}{4\pi r^2}, \tag{3.3}$$

where r is the radial distance to ds at angle ϑ.

The probability that a beta particle with its direction of motion within this solid angle will reach ds is given by the attenuation factor for the gaseous medium,

$$f = e^{-\nu\rho r}, \tag{3.4}$$

where ν is the single-collision mass absorption coefficient in air (cm^2/g), and ρ is the density of the medium (g/cm^3).

The maximum energy in the beta spectrum is used to determine the mass absorption coefficient in air for the beta continuum of energies. For single-collision theory, the apparent mass absorption coefficient is given by the empirical relation [25]:

$$\nu = 16(E_m - 0.036)^{-1.4}, \tag{3.5}$$

where E_m is the maximum energy in MeV.

Equations (3.2), (3.3), (3.4), and (3.5) are substituted into Equation (3.1), and the space integral is carried out for specified values of (r,ϑ). The equation for the incidence rate on ds is

$$R_\beta = C\int_\vartheta \cos^2\vartheta d\vartheta \int_r e^{-\nu\rho r(\vartheta)} dr \ , \tag{3.6}$$

where the limits for (r,ϑ) for a semi-infinite cylindrical chamber are

$$0 \leqslant r \leqslant R/\cos\vartheta \ , \tag{3.7}$$

and

$$0 \leqslant \vartheta \leqslant \pi/2 \ , \tag{3.8}$$

where R is the cylinder radius. Thus, the final equation for the incidence rate is

$$R_\beta = \frac{C}{\nu\rho}\int_\vartheta \cos^2\vartheta[1- e^{-\nu\rho R/\cos\vartheta}]d\vartheta \ . \tag{3.9}$$

The trapezoidal rule is used for the numerical integration of Equation (3.9) over the range of (ϑ). A copy of the program appears in Appendix A.

B. A Point Detector in a Rectangular Prism

The equation, in spherical coordinates, used to represent the incidence rate for a point on the base plane of a rectangular prism is

$$R_\beta = C\int_\vartheta\int_\varphi\int_r e^{-\nu\rho r} r^2 \sin\vartheta \frac{\cos\vartheta}{4\pi r^2} dr d\varphi d\vartheta \ . \tag{3.10}$$

Figure 3.2 shows the geometry used to relate a point detector to small rectangular regions on the wall of a finite rectangular prism. A point is selected in the prism base plane and rays are extended to intersect and form a rectangular region on the prism wall. The differential incidence rate due to the volume in this cone is then calculated by projecting the rectangular region normal to the rays extending from the base plane. An integration scheme for the differential angle ($d\theta$) is performed over all regions on the five prism walls to give the incidence rate for a point detector in a rectangular prism.

The computer program for a point detector in a rectangular prism was developed and used to check the results obtained from the program used to solve Equation (3.9). A copy of this program appears in Appendix B.

C. Finite-Area Plane Detector in a Rectangular Prism

An iterative process is used to determine the incidence rate for a finite-area plane detector in the base plane of a rectangular prism. The plane detector is approximated by a group of point detectors arranged on a grid covering the area of the detector. The incidence rate for the plane detector is determined by summing the incidence rates for this group of point detectors. The incidence rate for each point detector on the grid is determined by the method used to determine the incidence rate for a single point detector.

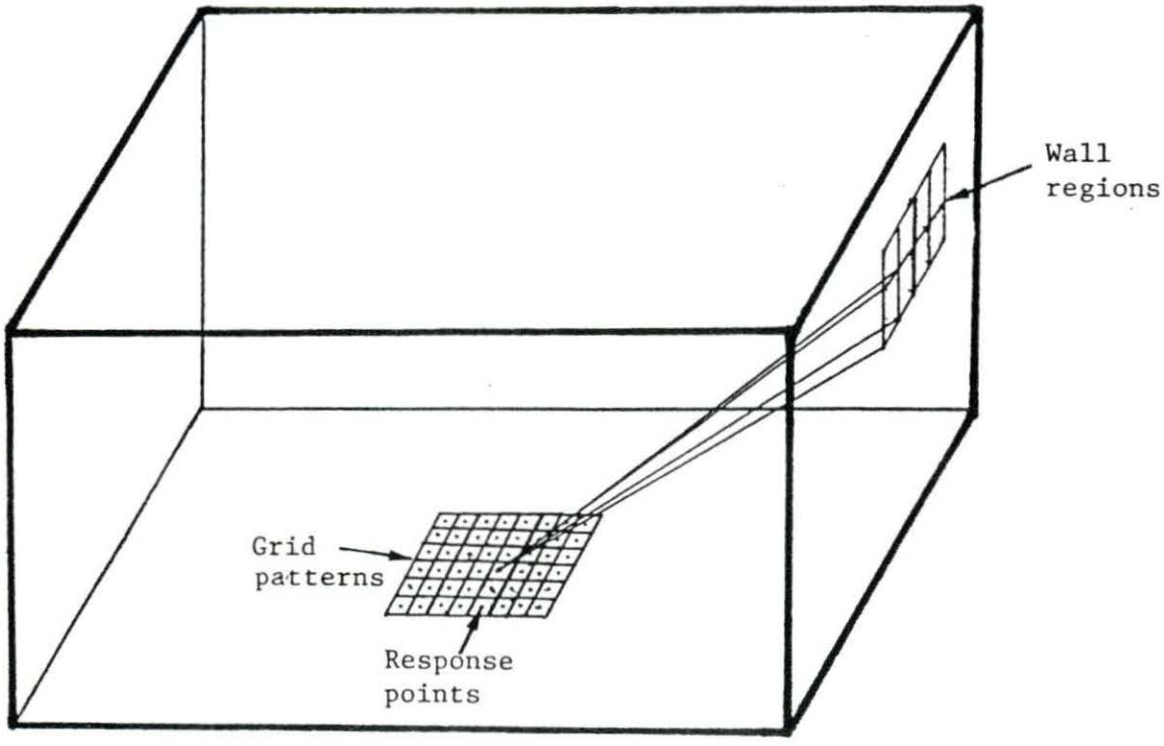

Figure 3.2. Geometry used for calculating the incidence rate for a point detector in a rectangular prism

D. Computational Analysis

1. Calculation of incidence rates

The results of calculations of the normalized incidence rates for the point detectors agreed to within 3 percent for a chamber radial distance of less than one meter. The normalized incidence rate is defined as the ratio of R_βs for finite and infinite chamber radial distances, where the chamber radial distance is defined as the distance from a central point in the chamber to the closest point on the chamber wall. The normalized incidence rate for the point detector in the rectangular prism was larger when compared with the normalized incidence rate for the point detector in the cylindrical chamber for radial distances less than one meter because of the additional activity in the edge area of the rectangular prism [26]. For radial distances greater than one meter, the normalized incidence rates of the point detectors agreed to within 0.1 percent.

Figure 3.3 shows the normalized incidence rates for both the point detector and finite-area plane detector of dimensions 90 x 250 mm. Figure 3.3 also shows that for radial distances less than one meter the normalized incidence rate for the finite-area plane detector was greater than for the point detector in a cylindrical chamber by up to 20 percent. Beyond one meter the normalized incidence rates for both detectors agreed to within 0.1 percent.

Figure 3.4 shows the normalized incidence rates for the noble gases of interest for the finite-area plane detector. The normalized incidence rates were thus dependent upon the incident beta spectrum.

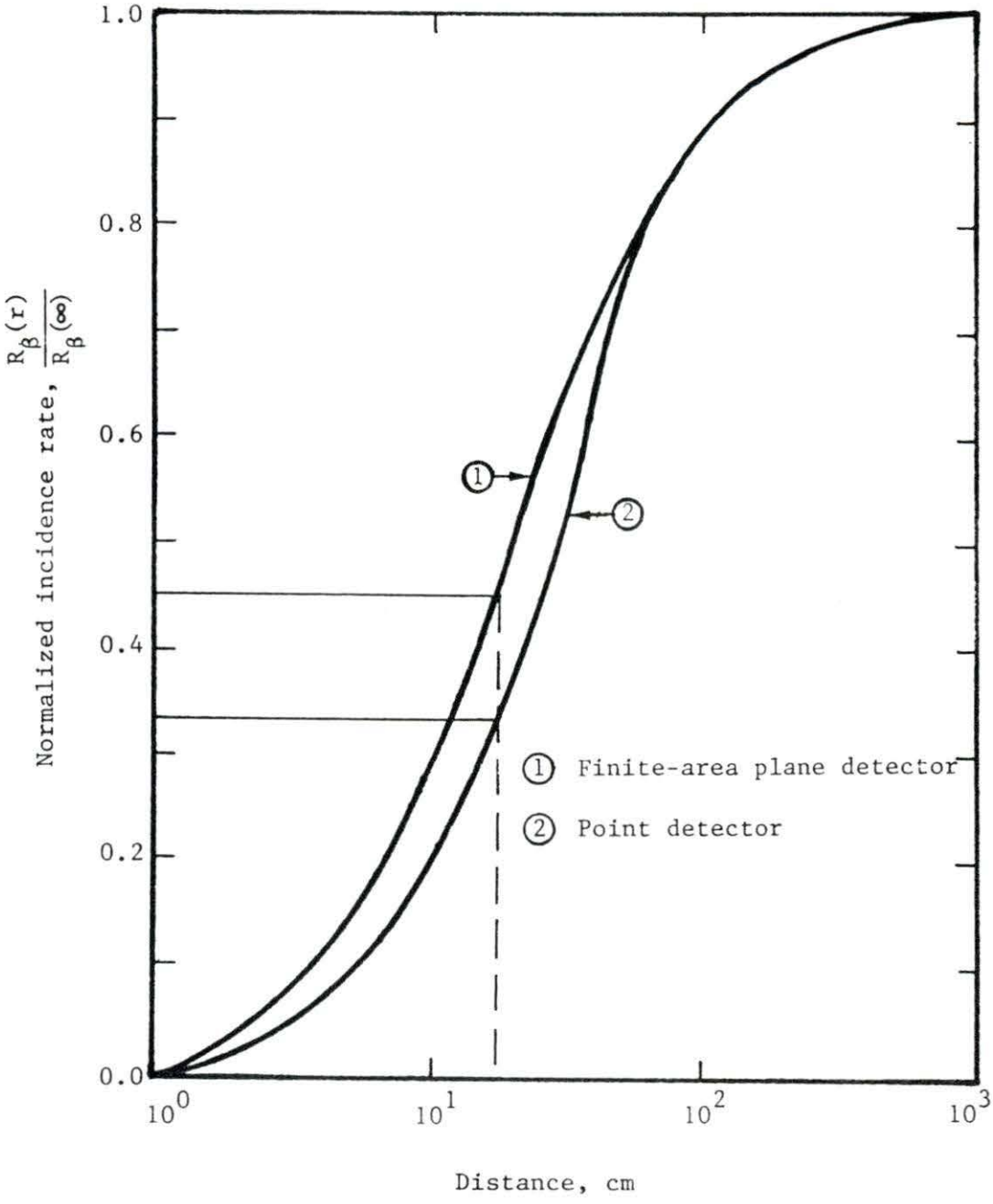

Figure 3.3. Normalized incidence rates for a maximum beta energy of 1.198 MeV (Ar-41) versus the perpendicular distance from the base-plane centroid to the chamber wall for a volume distributed source to a point detector and a finite-area (90 x 250 mm) plane detector. The dashed line corresponds to a perpendicular distance of 20 cm

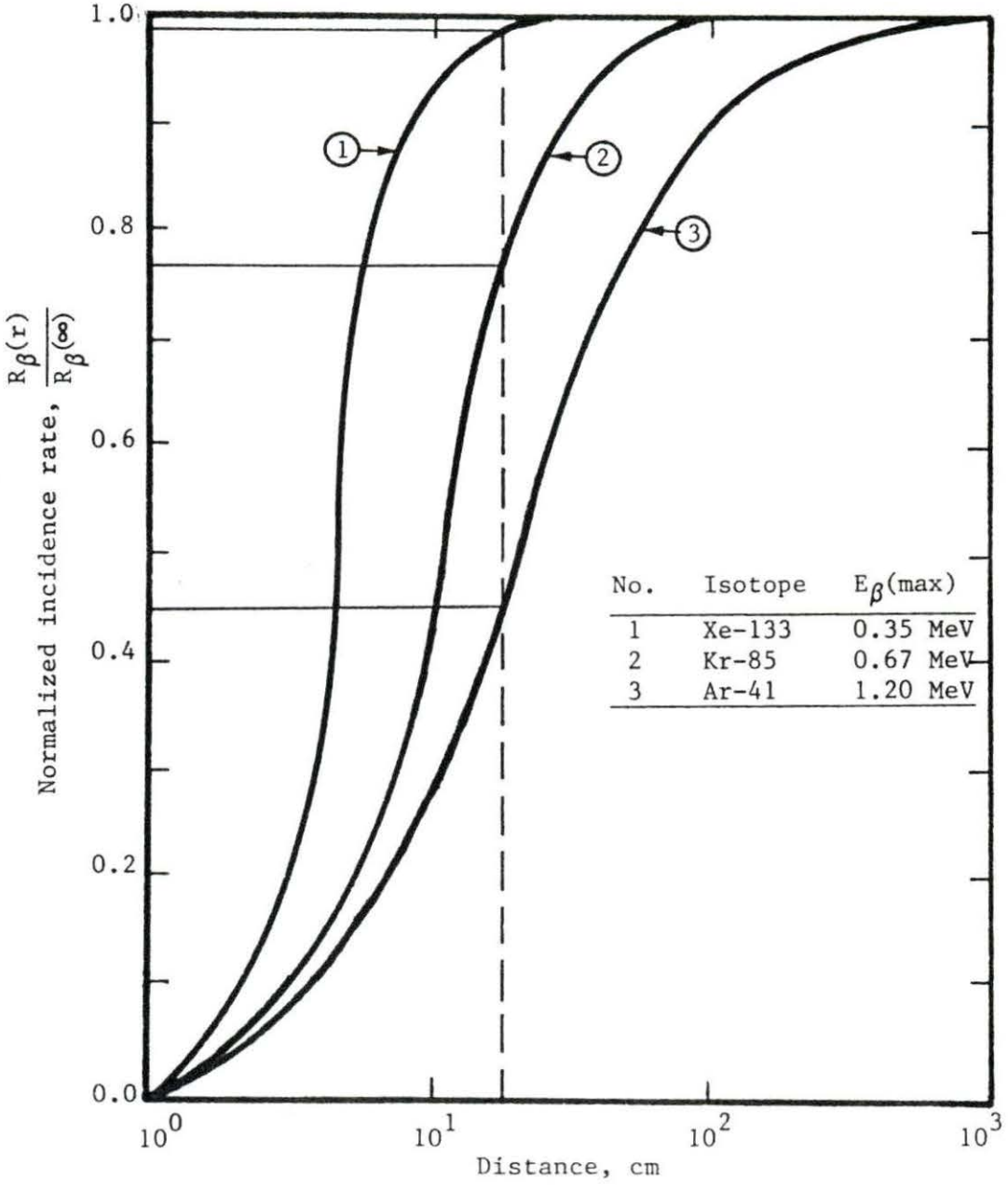

Figure 3.4. Normalized incidence rates for the noble gases of interest for the finite-area (90 x 250 mm) plane detector versus the perpendicular distance from the base-plane centroid to the chamber wall for volume distributed sources. The dashed line indicates a perpendicular distance of 20 cm

The choice of the nominal chamber radial distance will be presented in the apparatus and methods section.

2. Calculation of absolute detection efficiencies

The calculated argon-41 beta-gamma absolute detection efficiency is 1.34 percent for a finite-area plane detector of dimensions 90 x 250 mm centered in a 40 x 63 x 20 cm chamber. The absolute detection efficiency is the interaction efficiency multiplied by the probability of conversion of an interaction to a detectable signal. The interaction efficiency is the ratio of the incidence rate on ds, multiplied by the probability of absorption within the plate-type detector, to the number of particles per disintegration, where the degree of absorption is based on a mass attenuation coefficient.

The absorption factor for argon-41 beta radiation is assumed to be very close to 1.0, because the maximum range of argon-41 beta radiation in this detector material is the thickness of the plate-type detector, 6 mm. The absorption factor for argon-41 gamma radiation incident perpendicular to the 6.0 mm plate-type detector is 0.084 [27].

The conversion probability is assumed to be 1.0 for argon-41 beta and gamma radiation for ease of calculation, since its calculation is beyond the scope of this study.

The interaction efficiency is calculated for only one side of the plane detector, as each side of the plane detector is identical and thus will have the same efficiency. The 90 x 250 mm plane detector, shown in Figure 3.2, is centered in a 40 x 63 cm plane. This is the

base plane of one 40 x 63 x 20 cm symmetrical prism. The incidence rates are calculated (program in Appendix B) using a unit emission rate per volume for beta and gamma volume sources. The calculated incidence rate for a one beta/cc/second source is 614 betas/second. The interaction efficiency (1.22 percent) is the ratio of the incidence rate to the source emission rate (50,400 betas/second), multiplied by the probability of absorption (1.0) within the plate-type detector. Assuming a conversion probability of 1.0 gives an absolute beta detection efficiency of 1.22 percent.

The calculated incidence rate for one gamma/cc/second source is 720 gammas/second. The interaction efficiency (0.12 percent) is the ratio of the incidence rate to the source emission rate (50,400 gammas/second), multiplied by the probability of absorption (0.084) within the plate-type detector. Assuming a conversion probability of 1.0 gives an absolute gamma detection efficiency of 0.12 percent. Therefore, the argon-41 beta-gamma absolute detection efficiency for the plate-type detector is estimated to be 1.34 percent.

IV. EXPERIMENTAL APPARATUS AND METHODS

A. Sampling Chamber and Detector Design

1. The sampling chamber

The choice for the nominal chamber radial distance was based on the percentage increase in the normalized incidence rate for the semi-infinite cylindrical chamber model which gives a normalized incidence rate on a point detector exposed to argon-41 of approximately 34 percent of an infinite approximation, i.e., a cylindrical chamber of infinite dimensions. A cylindrical chamber with a radial distance larger than 20 cm will incur an added cost for construction as well as the possibility of causing non-homogeneous conditions to occur within the increased volume. Flow conditions within the chamber are laminar to 150 lpm [28], suggesting that homogeneous conditions exist within this limit.

The normalized incidence rate for a plate-type detector in a rectangular prism with a 20 cm radial distance, as shown in Figure 3.3, is about 41 percent. The difference between the larger normalized incidence rate for the plate-type detector and the point detector is attributed to the additional active volume within the edges of the rectangular prism.

A rectangular prism was constructed of Plexiglas with dimensions of 40 x 40 x 63 cm with a detector surface-to-chamber-wall distance of 20 cm. This radial distance was preserved throughout the entire chamber to ensure homogeneous flow conditions. The construction of the chamber allowed flow patterns to be observed. Figure 4.1 shows the sampling chamber that

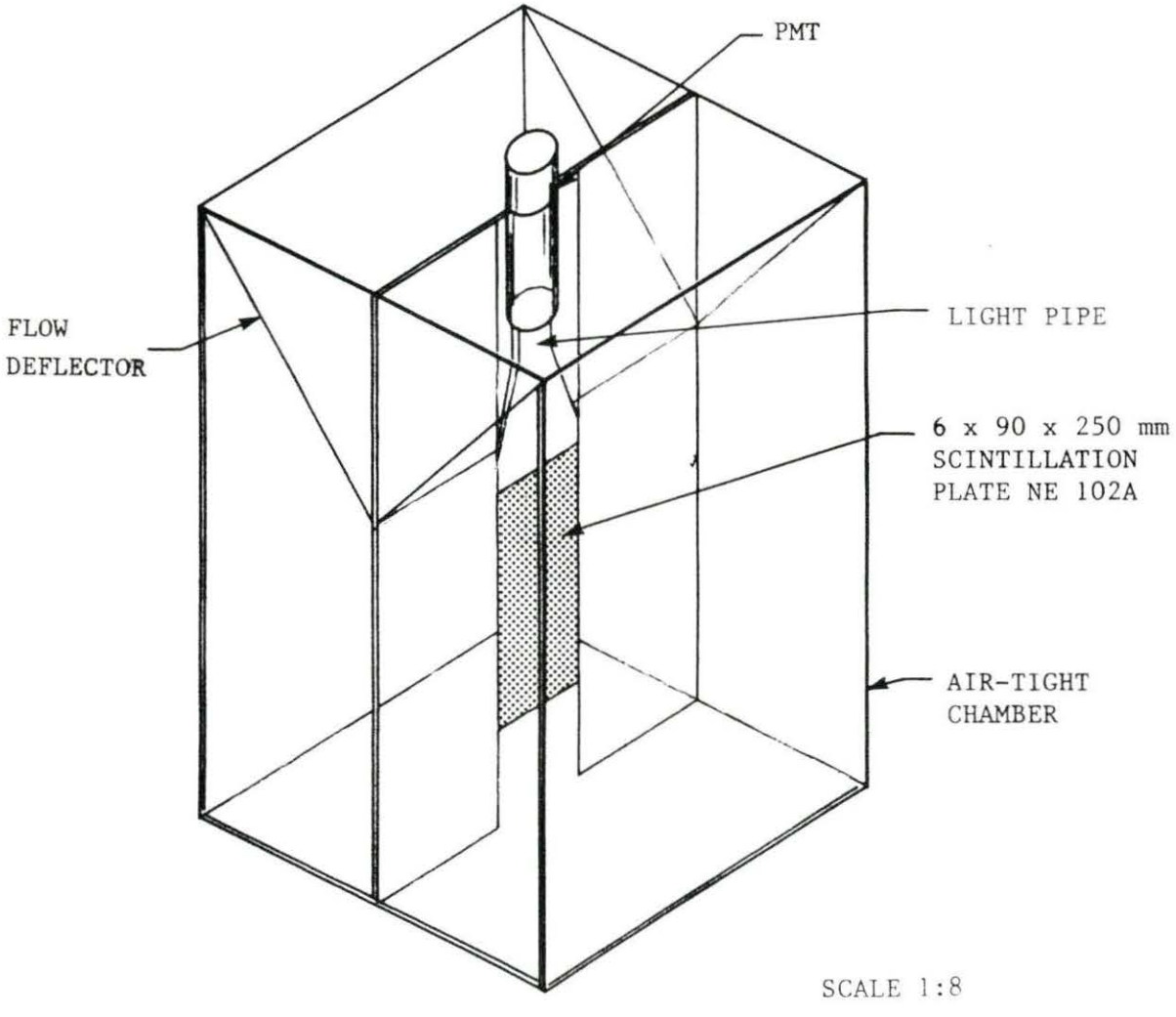

Figure 4.1. Noble gas sampling chamber

was designed to complement the shape of the detector. The plate-type detector was positioned in a grooved track supported by two side plates, thus sectioning the chamber into two equal volumes. Flow deflectors were used to direct air movement across the surface of the detector to the chamber base and up the reverse side to the chamber exit. To minimize corrections to measurement data for chamber pressure differentials, an inlet tube of 7.62 cm (3 in.) i.d. was used to permit unrestricted flow into the chamber. An inlet filter, MSA type H filter cartridge, was used to eliminate particulates and dust from interacting with the system. This filter cartridge can remove particles down to 0.3 microns with 99.7 percent efficiency [29]. The pressure drop across the filter was less than 12 mm (1/2 in.) Hg at a flow rate of 70 lpm. The chamber exit consisted of a 1.27 cm (1/2 in.) i.d. tube 16 cm (6.3 in.) long with a rotameter positioned on a flange at the exit. Full laminar flow was established after 12.7 cm (5 in.) of inlet tube length. At this point, a pressure tap was permanently fixed in the bottom wall of the exit tubing. The recommended wall-to-tap ratio of greater than 0.5 but less than 6.0 [28] was noted. The tap diameter was 1.59 mm (1/16 in.) with a wall thickness of 2.54 mm (1/10 in.), thus giving a wall-to-tap ratio of 1.6. In this region, the difference between the observed and true flow rates was less than 0.1 percent for measured flow rates in the range from 5 lpm to 70 lpm.

2. The plate-type detector

NE 102A, a beta-gamma sensitive scintillating plastic, was selected as the detector for the monitoring system. This material has good light output (65 percent of anthracene), good light transmission

(2.5 meter attenuation length), and a refractive index of 1.581 which is close to the index for a Plexiglas light pipe. This detector material is relatively inexpensive and has a high count rate capability due to its extremely fast pulse decay time.

The dimensions of the plate-type detector selected for this study were 90 x 250 x 6 mm. The detector thickness of 6 mm corresponds to the range of 1.3 MeV beta particles in this material. This specific energy is the largest maximum energy encountered from the noble gases of interest. The 250 mm detector length was chosen after reviewing available data from studies of annular detectors [7]. Detection sensitivities for different beta energy spectra were shown to saturate for increasing lengths of annular detectors of fixed diameter. The saturation length was shown to be approximately 250 mm for a 1.3 MeV beta energy spectrum. The best length for the plate-type detector was estimated based on annular detector data, because response information for plate detectors was not available in the literature reviewed. The 250 mm length was a reasonable estimate, but it may not be the actual saturation length required for argon-41 monitoring. The saturation length is very important since it affects the length at which background has minimal influence on source measurements.

The width of the detector was chosen for maximum efficiency in light transmission through the light pipe from the detector to the photo-multiplier tube (PMT). The cross-sectional area of the light pipe was maintained constant and sharp bends were avoided in the fabrication process so that the light pipe could theoretically transmit all light

that entered within the critical angle of the detector end. For this particular arrangement, three Plexiglas strips, each 30 x 170 x 6 mm, were bonded on-edge at one end, then heated until flexible enough so that each could be smoothly twisted 90° to converge face against face, forming an 18 x 30 mm rectangular end to spread the light over the photocathode of the PMT. The detector-light pipe unit was wrapped in aluminum foil (10 mg/cm^2) to reflect scintillation light produced in the detector. Black electrical tape (20 mg/cm^2) was wrapped around the aluminum to immobilize it. The tape and foil attenuated extraneous light sources as well as low-energy beta particles. The total absorber thickness (30 mg/cm^2) was sufficient to stop betas with energies below 0.12 MeV. Therefore, high-efficiency beta detection occurred for energies greater than 0.12 MeV and less than 1.3 MeV.

A 5.08 cm (2 in.) PMT was chosen for its low dark current, and its low cost. The tube was positioned in a PMT housing and optically coupled to the light pipe with silicone grease. Mu-metal was wrapped around the tube and was kept at cathode (ground) potential to reduce interference from stray magnetic fields.

B. System Components

A block diagram of components for the detection system is displayed in Figure 4.2. The electronic components for the system were the photomultiplier tube (PMT), preamplifier (P/A), high voltage bias supply (HV), amplifier (AMP), counter/timer (C/T), and multichannel analyzer (MCA). A beta particle interacting with the plate-type detector produced a pulse of light. The light pulse was converted to a charge pulse by the PMT.

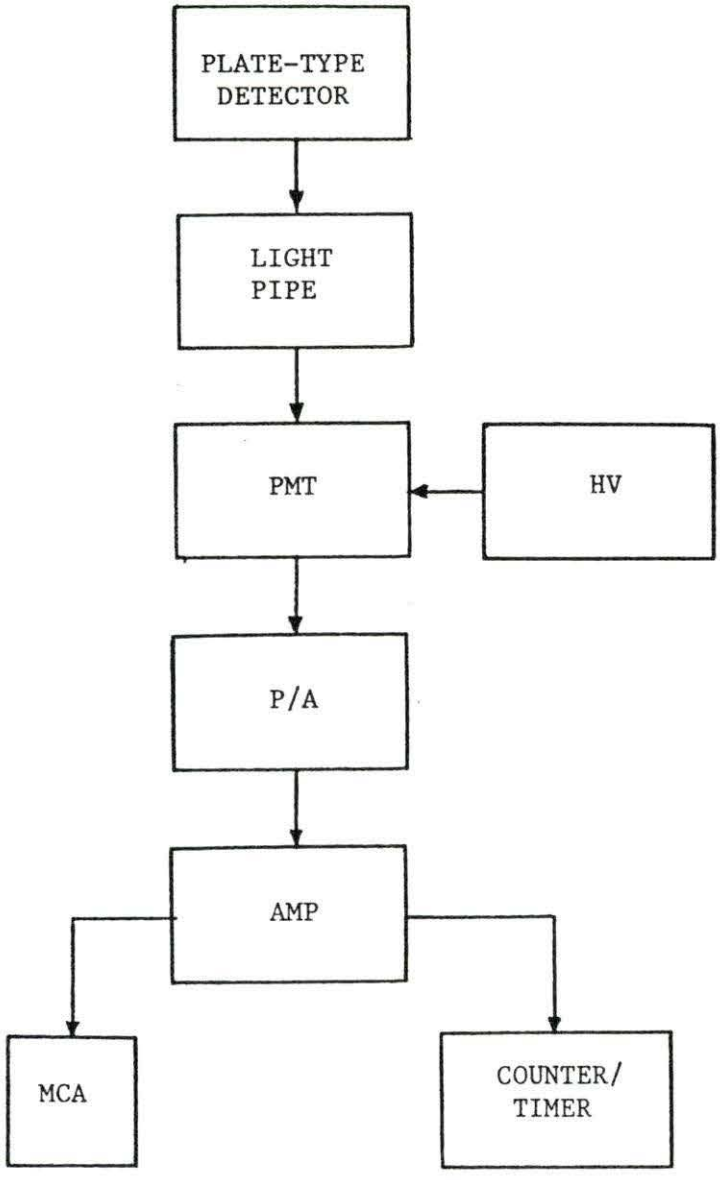

Figure 4.2. Block diagram of the detection system

The charge pulse was transformed into a voltage pulse by the P/A, amplified and shaped by the AMP, and recorded by the C/T, or the MCA. Table 4.1 provides a list of the equipment needed to operate the detection system.

Table 4.2 lists the mechanical components associated with the operation of the sampling chamber. The pump was operated over a continuous range from 5 lpm to 70 lpm. The rotameter was calibrated for various pressure differentials with a wet test meter (WTM). A precision manometer was used to monitor pressure differentials in the sampling chamber. Figure 4.3 shows the arrangement of these components for operation in the system.

C. Testing of the Monitoring System

1. Detector and electronic components

The detector and electronic components were tested to determine the following:

1. Bias voltage to the PMT at which the background rate had minimal effects on the net rate;
2. Absolute detection efficiencies for the response of the plate-type detector to both beta and gamma radiation;
3. Beta-to-gamma detection ratios;
4. Light collection efficiency effects on the integral counts and pulse heights for beta radiation;
5. Spectral response to both beta and gamma radiation for determining the degree of energy discrimination.

Table 4.1. The components for the detection system and associated electronics

Component	Make	Model
Detector	EMI	NE 102A
Light pipe	Local fabrication	N/A
PMT	EMI	9856KB
PMT housing	EMI	B-256
P/A	Canberra	805
AMP	Canberra	816
HV	Fluke	412B
C/T	Canberra	1772
MCA	Canberra	30

Table 4.2. Mechanical components associated with the sampling chamber

Component	Make	Model
Pump	Gast	RAP-1
Wet test meter	Precision Scientific Co.	63111
Rotameter	Dwyer	RMA-24-SSV
Mercury manometer	Merian Instruments	SC-6446

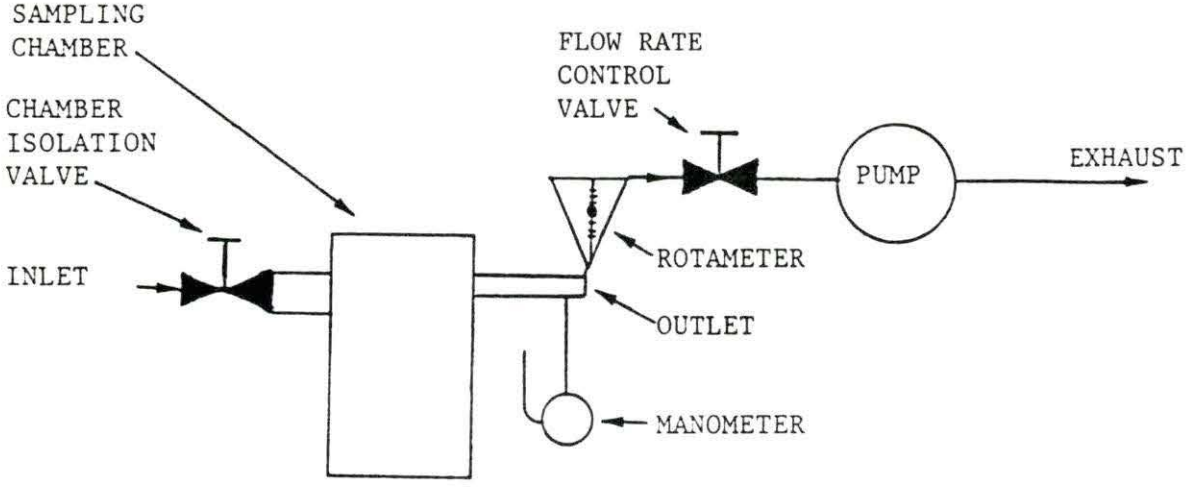

Figure 4.3. Arrangement of sampling chamber and mechanical components for operation of the monitoring system

A PMT bias voltage was selected to maximize the net rate and minimize the background rate. For this operation, it was necessary to apply a positive bias voltage to the anode of the PMT in the range from +600 volts to +1400 volts. The latter voltage was the operating limit of the PMT. The net rate and background rate were observed to determine the PMT bias voltage at which the background rate had minimal effects on the net rate.

Experimental absolute detection efficiencies were determined for beta, gamma, and conversion electron point sources at various perpendicular distances from the geometric center of the plate-type detector. The absolute detection efficiency is the ratio of the net rate to the source rate (certified source emission rate). This test was used to observe gamma detection efficiencies, and beta detection efficiencies with most probable energies above and below the 0.12 MeV cutoff energy.

Beta-to-gamma detection ratios were then determined by calculating the ratio of the beta efficiency to the gamma efficiency for beta-gamma emitting sources.

Light collection efficiency effects on the total counts and pulse heights were determined by placing a calibrated beta source at various positions on the surface of the plate-type detector. These tests indicated that the plate-type detector length was adequate for argon-41 detection and helped to define the degree of energy discrimination.

The spectral response to both beta and gamma radiation was needed to also determine the degree of energy discrimination. Here, various beta and gamma sources were positioned 15 mm from the light-pipe end

and counted for 4000 seconds. Spectra were then obtained from a MCA for each source (in background) to identify specific areas of interest, i.e., peaks, endpoints.

2. Sampling chamber

The sampling chamber was tested to determine the following:

1. The existence of air leakage from the chamber;
2. The flow patterns within the chamber;
3. The elapsed time for a 12 ml smoke sample to homogenize in the chamber.

A test plate and light pipe were inserted into the chamber for testing purposes. A silicon seal was then placed on all joints to reduce air leakage. Smoke from a $SnCl_4$ smoke stick was blown into the chamber for the leak test. The chamber was pressurized to +30 mm Hg above atmospheric pressure to reveal the exact locations of air leakage. The prominent leaks were plugged, and the chamber was rechecked for any small leaks.

Vacuum valves were installed on the inlet and outlet of the chamber to keep the pressure constant during leakage tests. With the inlet closed, the outlet remained open to the pump until a chamber pressure differential of -30 mm Hg was registered by the manometer. The outlet was then closed, and the chamber pressure was observed for ten minutes. If the manometer level remained constant during the testing period, air leakage was assumed not to occur.

The smoke test was also used to study flow patterns within the chamber to ensure homogeneous conditions. The test was conducted by

connecting a smoke stick in-line directly to the chamber for flow rates from 5 lpm to 70 lpm.

A 12 ml smoke sample was injected into the system with a syringe to simulate the transfer of calibration gas to the sampling chamber. While the pump recirculated the air-smoke mixture, the mixing time was determined. This was accomplished by ascertaining the length of time necessary for the air-smoke mixture to homogenize within the chamber. This mixing time was used to insure that homogeneous conditions existed during calibration of the monitoring system for a release of argon-41 from the source vial.

D. Calibration of the Monitoring System

1. Plate-type detector energy calibration

Energy calibration was needed to maximize the net rate for argon-41 and limit the background rate. The maximum net rate occurred when a pulse height equivalent to the full-memory channel was obtained from the argon-41 gas. Energy calibration was accomplished by placing various beta and gamma calibrated sources on the symmetry line of the plate-type detector, 15 mm from the light pipe edge. This particular location was chosen because measured pulse heights were found to be greatest in this region.

2. Argon-41 calibration factor

A calibration factor (μCi/cc/cpm) for a known release of argon-41 was sought which related the counting rate obtained by the system to the concentration of activity in the chamber. A Plexiglas source vial, shown

CROSS SECTIONAL VIEW

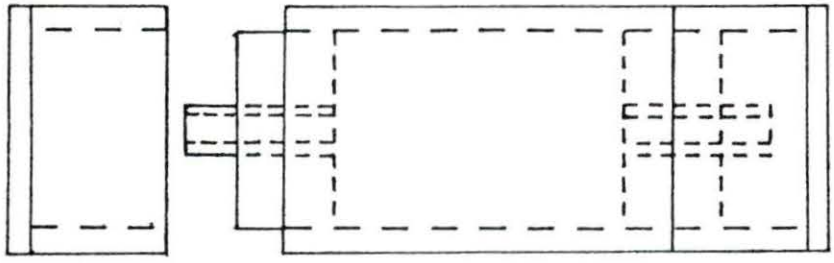

SCALE 1:1

Figure 4.4. Plexiglas source vial to hold P-10 counting gas (90 percent argon, 10 percent methane)

in Figure 4.4, was filled with P-10 counting gas by purging distilled water from its active volume with the gas pressure set at 0.5 psi. The vial was filled gradually to reduce the formation of water residue on the inside vial walls. If residue remained after the vial was filled, the vial was tapped with a soft object to cause the remaining water droplets to collect at the bottom of the vial. The P-10 gas line could be turned on just enough to force the remaining water from the vial. The inlet to the vial, at which the P-10 source line was inserted, was pinched and removed at the same time the outlet was pinched to prevent the escape of P-10 gas. Then, a cap was placed over each end to protect against damage to the protruding tube ends.

The vial of P-10 gas and a gold foil in a 20 mil cadmium cover were activated in the pneumatic irradiation facility of the Iowa State research reactor. The gold foils were used to provide data for normalizing argon source activities produced during multiple runs. To ensure reproducible data, the same rabbit and cadmium cover were used throughout the calibration process.

The activities of the gold foils were measured for 5 minutes each over a period of 10 days. A NaI(Tl) detector, located in a lead cave with a source-to-detector distance of 10 cm was used. The NaI(Tl) detector was checked for fluctuations by counting a Cs-137 source before counting each gold foil to correct the gold activities on a day-to-day basis.

After energy calibration, a sample of P-10 gas, irradiated in the vial to produce argon-41, was connected in-line to the monitoring system.

The pump was allowed to recirculate the chamber exhaust back to the inlet at a flow rate of 70 lpm for the time required to reach homogeneous conditions in the sampling chamber.

The counts accumulated in a MCA operating in the multichannel scaling (MCS) mode, reached saturation before the end of the mixing period. If equilibrium did not occur, there was air leakage from the chamber. After the mixing period, the pump was shut off, and both inlet and outlet valves were closed. The counting room was continuously monitored with a NaI(Tl) detector to determine if leakage of argon-41 from the chamber occurred.

Monitoring of the calibration gas activity in the chamber was accomplished by counting for 5 minutes every 10 minutes. The decay of argon-41 was measured and plotted to verify the 1.83 hour half-life, and to determine the initial counting rate from the source at the end of the irradiation time. The calibration factor was determined for argon-41 by dividing the calculated activity concentration of argon-41 in the chamber by the counts per minute at the end of the irradiation time. The argon-41 concentration was the calculated activity in the vial divided by the total volume of the system components. Table 4.3 lists the system components and their respective volumes.

The first set of calibrations for argon-41 was for total beta and gamma interactions. To determine the magnitude of each interaction detected, a second calibration for gamma interactions was performed with a 605 mg/cm^2 Plexiglas absorber over both sides and the bottom of the plate detector to attenuate beta radiation. This was needed to

Table 4.3. Total volume for components of the monitoring system

Component	Volume (cc)
Chamber	97,600
Vial	19.6
Inlet	2120
Outlet	1900
Tubing	32
Pump	214[a]
Rotameter	11.4
Total	101,897

[a]Manufacturer's estimate.

verify the beta-to-gamma detection ratio for a volume source of argon-41.

After normalization of the calibration factors using gold activities, a mean calibration factor was calculated and used to convert the counts per minute of an experimental run to an argon-41 concentration in μCi/cc.

3. Flow rate calibrations

Errors arose as a consequence of the Dwyer rotameter operating at conditions of pressure other than standard. Any pressure drop across the sampling chamber automatically resulted in the Dwyer rotameter operating at reduced pressure. Before flow calibration began, the wet test meter (WTM) was prepared and tested to ensure the manufacturer's specified accuracy of ½ percent. Procedures for preparation of the WTM are given in Appendix C.

Problems also arose in the application of corrections to the WTM measurement data because the standard specifying the use of the gas correction factor was discontinued. ASTM was unable to provide a standard for applying gas correction factors to WTM data [30], and therefore, the correction factor was omitted in all flow rate corrections. A derivation of the correction equation for WTM flow rates is presented in Appendix D.

Calibration of the Dwyer rotameter for various pressure differentials was performed by varying pump flow rates from 5 lpm to 30 lpm, and throttling the inlet and outlet valves. To avoid large errors in WTM measurements, the calibration system was allowed to operate for at least

30 minutes after a change had been made in the chamber pressure. Sampling times of 2-3 hours were needed to record a large sample volume and reduce errors in the recording of the sampling time.

E. Activity Measurements

The activity measurements consisted of using the plate-type detector to measure argon-41 activity concentrations at selected points near the UTR-10 reactor during and after operation at one-half maximum power for one hour. The section of the building housing the reactor was closed off to limit the entry of fresh air and the escape of building air during measurement periods. Entrance into this area was restricted for at least 6 hours after the reactor reached the selected power level. This was done in order to determine the maximum activity of argon-41 in the reactor area. The counting room was also isolated from the reactor area so that argon-41 released during the reactor operation would not leak into the room and directly affect background measurements of the monitoring system. Argon-41 present in the counting room raises the background level, and complicates sampling procedures since background has to be monitored directly after each sample is counted.

A 15.24 meter (50 ft.) sampling line, 6.35 mm (0.25 in.) i.d. Tygon tubing, was connected to the chamber inlet and extended to the reactor area. The exhaust from the sampling chamber was pumped through a line passing through an adjacent window. A NaI(Tl) detector, shielded from the sampling chamber by 5 cm (2 in.) of lead, was positioned to monitor background variations within the room. This detector was used to determine, by energy discrimination, if argon-41 entered the sampling

room.

Two methods of detection were used to sample air from the reactor area. The first method was a dynamic (on-line) process in which monitoring was accomplished with a continuous flow of air at 10 lpm through the chamber for counting times of 5 minutes. The second method was a static (off-line) process in which an air sample was drawn into the chamber and held by closing the outlet and inlet valves. This method was used to monitor very low concentrations, and long sampling times ranging from 5 minutes to 20 minutes were required.

Background measurements were taken just after the specified reactor power level was achieved and during the activity measurement period. This was accomplished by disconnecting the sample line and purging the chamber of all radioactive contents. The inlet flange plate was removed to permit operation at 70 lpm in a near-zero pressure differential. After 7 minutes, the pump was disconnected and the sampling chamber was sealed. Operating the system at 70 lpm for 7 minutes purged the chamber volume 5 times. This was needed to ensure that all argon-41 was expelled from the chamber, and that a true background count was recorded. Counting times of 5 minutes were used to obtain background measurements.

In taking data to determine argon-41 concentrations, the system was operated in the dynamic mode for at least 12 minutes before a true count could be recorded. This was due to the transport time required for a sampling taken through the inlet line to reach the chamber exit. Once the system reached equilibrium, the pump was disconnected and the inlet and outlet valves closed to establish the static mode. Counting in the

static mode was done immediately after the system valves were closed to limit corrections for decay of argon-41 in the sampling chamber. The concentration of argon-41 at the sampling location was determined by multiplying the net counting rate obtained from the monitoring system by the calibration factor.

V. RESULTS

A. Testing of the Monitoring System

1. Detector and associated components

The results of varying the bias voltage and its effect on the net rate and background rate are shown in Table 5.1. A net rate plateau region was observed in the range of bias voltage from +900 volts to +1100 volts. A bias voltage to the PMT of +900 volts was chosen because the ratio of the net rate to the background rate was the highest (15.3) in the plateau region.

Experimental absolute detection efficiencies for point sources emitting beta and gamma radiation at various perpendicular distances from the geometric center of the plate-type detector are shown in Table 5.2. The absolute detection efficiency is the ratio of the number of particles or rays detected to the number of particles or rays emitted from the source.

An experimental investigation of absolute detection efficiencies for beta radiation determined that the 30 mg/cm^2 absorbing wrap allowed high efficiency beta counting for the particular beta energies of interest. Experimental absolute detection efficiencies for the plate-type detector were greater than 27 percent for beta radiation from Bi-210 and Cl-36. For Tc-99 and C-14, the absolute detection efficiencies were very low, because their most probable beta energies were below the 0.12 MeV cut-off energy of the detector. Absolute beta detection efficiencies, reported in the literature reviewed, for a 4.7 cm (1.85 in.) diameter, 3 mm thick,

Table 5.1. Net rate and background rate as a function of bias voltage to the PMT. A 53.4 nCi Bi-210 beta source (E_{max}=1.17 MeV) was on the geometric center of the plate-type detector mounted outside of the sampling chamber for 5 minute sampling times

Bias (volts)	Net Rate (cpm)	Background Rate (cpm)	Net Rate / Background Rate
700	18225	846	21.5
800	33209	1670	19.9
900[a]	47599[b]	3104	15.3
1000	51050[b]	5361	9.5
1100	54752[b]	7489	7.3
1200	66208	12217	5.4
1300	99764	26650	3.7
1400	178182	44827	4.0

[a]Selected bias voltage.

[b]Net rate plateau region.

Table 5.2. Absolute detection efficiencies, in percent, for point sources at specified distances perpendicular to the centroid of the plate-type detector and to the surface of a 3 x 3 in. NaI(Tl) detector for 15 minute sampling times

Source	Activity (nCi)	Radiation	Energy[a] (MeV)	Efficiency (%) 0 mm	20 mm	40 mm
NE 102A PLASTIC						
Bi-210	53.4	Beta	1.170	29.3	23.1	17.3
Cl-36	31.0	Beta	0.714	27.7	22.8	17.3
Cs-137[b]	30.0	Beta	0.514	13.3	6.09	3.75
Co-60[b]	83.0	Beta	0.310	0.85	0.49	0.30
Tc-99	55.7	Beta	0.292	0.84	0.59	0.46
C-14	113.0	Beta	0.115	0.11	0.04	0.00
Co-60	83.0	Gamma	1.173, 1.332	3.91	1.43	0.72
Cs-137	30.0	Gamma	0.662	4.64	1.80	1.01
NaI(Tl)						
Co-60[c]	N/A	Gamma	1.173, 1.332	30.5	11.5	6.00
Cs-137[c]	N/A	Gamma	0.662	37.0	14.0	7.30

[a]Maximum energy for beta radiation.

[b]Gamma detections subtracted.

[c]Efficiencies from Heath manual [31].

NE 102A detector wrapped in a 6.9 mg/cm^2 absorber of aluminum foil ranged from 5.15 percent for C-14 to 45.6 percent for Bi-210 [6].

Experimental absolute detection efficiencies for Co-60 and Cs-137 indicated that the plate-type detector yields low efficiencies for gamma radiation. No absolute detection efficiencies for gamma radiation were reported in the literature reviewed for NE 102A detector material.

Predicted absolute detection efficiencies for beta radiation from the noble gases of interest were determined from Figure 5.1. This figure displays measured absolute detection efficiencies, taken from Table 5.2, for point sources emitting beta radiation as a function of the maximum beta energy. The absolute detection efficiencies for Xe-133, Kr-85, and Ar-41 are estimated to be 1.2, 25.6, and 29.4 percent, respectively.

Absolute detection efficiencies for gamma radiation from point sources of the noble gases of interest were estimated for the plate-type detector. This was accomplished by assuming a linear relationship between gamma efficiencies for the plate-type detector and known gamma efficiencies for a NaI(Tl) detector [31], because the ratios of the absolute detection efficiencies for both detectors for Co-60 and Cs-137 gamma sources (Table 5.2) agreed within 5.0 percent. The ratio of absolute detection efficiencies for the two detectors was 7.86. Absolute detection efficiencies were determined by dividing known NaI(Tl) efficiencies by 7.86. Thus, the calculated absolute detection efficiencies for point sources emitting gamma radiation from Xe-133, Kr-85, and Ar-41 (on the geometric center of the plate-type detector) are estimated to be 6.36, 5.09, and 3.82 percent, respectively.

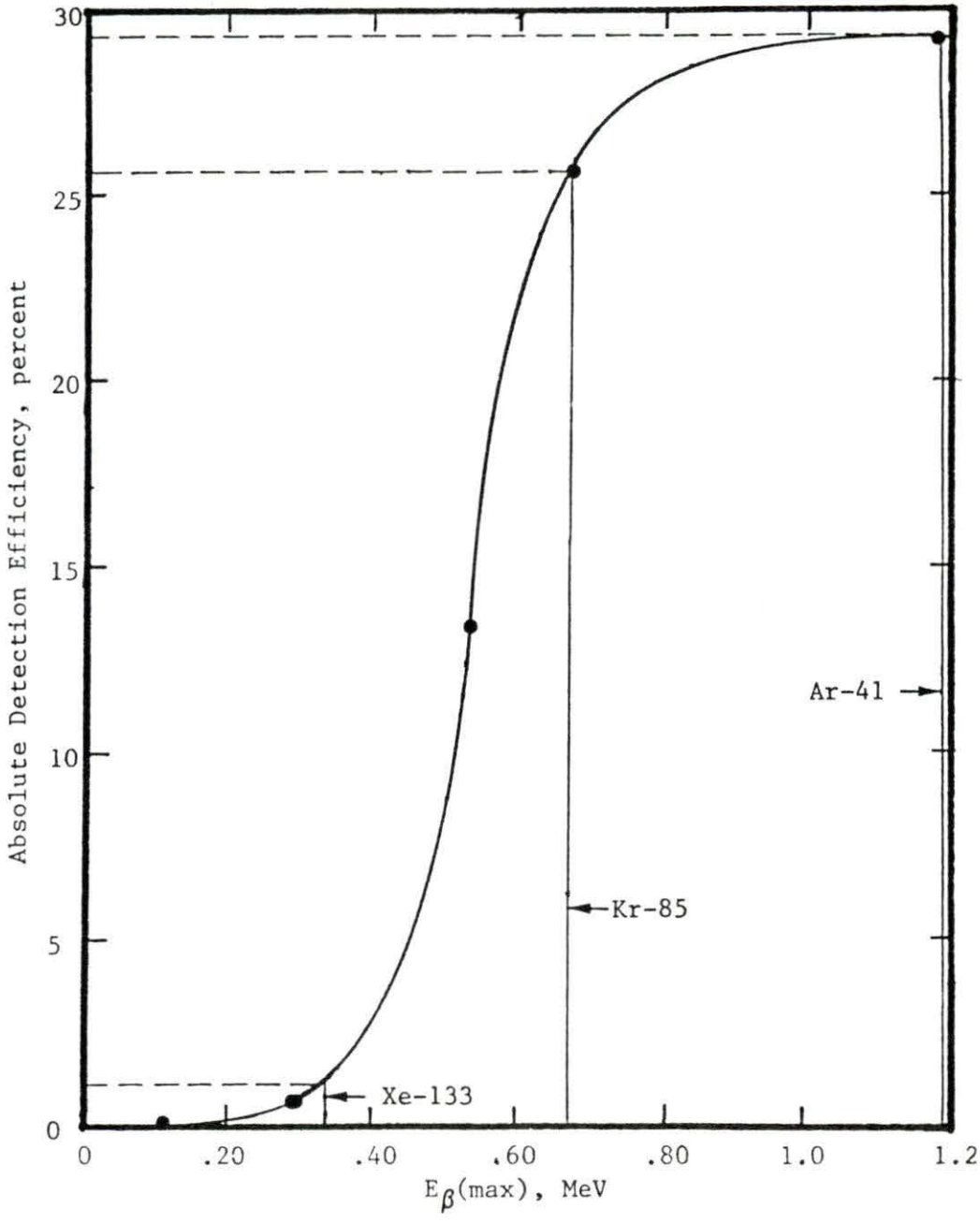

Figure 5.1. Absolute detection efficiencies as a function of the maximum beta energy for point sources positioned on the geometric center of the plate-type detector. The dashed lines indicate the absolute beta detection efficiencies for maximum beta energies corresponding to Xe-133, Kr-85, and Ar-41 (solid lines)

Beta-to-gamma detection ratios were calculated and compared to experimentally determined values. The beta-to-gamma detection ratio is the ratio of the beta and gamma detection efficiencies multiplied by the ratio of their emission probabilities. Experimental beta-to-gamma detection ratios were determined by placing thin beta absorbers between the source and the detector to obtain a gamma net rate and a beta-gamma net rate. The beta-to-gamma detection ratio is the ratio of the beta net rate to the gamma net rate. Experimental and calculated beta-to-gamma detection ratios are shown in Table 5.3. The beta-to-gamma detection ratio was very large for Kr-85 (1257) because this isotope rarely emits gammas (0.41 percent). Xe-133 has a very low ratio (0.19) because its most probable beta energy was below 0.12 MeV. For Ar-41, the calculated beta-to-gamma detection ratio was 7.69. The calculated and experimental beta-to-gamma ratios show that the plate-type detector (in the 30 mg/cm^2 absorbing wrap) is adequate for detection of beta radiation emitted from krypton-85 and argon-41.

Previous investigations of light transmission in plastics show that variations in the light collection efficiency can dominate the energy resolution [32]. The light collection efficiency is the ratio of scintillation light emitted when an ionizing particle transverses the detector material to the scintillation light collected by the PMT. The uniformity of the light collection efficiency determines the variations in the signal pulse height as the position of the particle interaction is varied throughout the plate-type detector. Uniform light collection efficiency assures that all events that deposit the same energy, regardless of the interaction position, would produce the same signal pulse height.

Table 5.3. Beta-gamma detection ratios for beta-gamma point sources based on 15 minute sampling times with sources resting on the centroid of the plate-type detector

Isotope	Energy (MeV) Beta[a] (Emission probability, %)	Gamma (Emission Probability, %)	Beta Stopping Thickness[b] (mg/cm^2)	Beta-gamma detection ratio
Co-60	0.31 (100)	1.17, 1.33 (100, 98.8)	81	0.12[c]
Cs-137	0.514 (94)	0.662 (84.8)	173	3.50[c]
Au-198	0.961 (98.9)	0.411 (99.0)	423	4.04[c]
Ar-41	1.198 (99.9)	1.29 (99.9)	526	7.69[d]
Kr-85	0.670 (99.6)	0.514 (0.4)	260	1252[d]
Xe-133	0.347 (99.3)	0.081 (35)	98	0.19[d]

[a]Maximum energy.

[b]Values from Kaplan [33].

[c]Observed values on plate-type detector centroid.

[d]Calculated values based on efficiencies and emission probabilities.

The effects of the variation in the light collection efficiency were experimentally investigated by observing pulse heights as a function of the source position on the plate-type detector. Figure 5.2 displays the relative pulse height of the most probable beta energy for a Bi-210 point source as a function of the source position along the centerline of the plate-type detector. The relative pulse height dropped approximately 27 percent (approaching an asymptotic value) between source positions at 15 and 250 mm from the light pipe end.

Because of the reduction in pulse heights as the source interaction postion is varied on the plate-type detector, a reduction in counting rates could also occur since low amplitude pulse heights could be reduced below counting windows. Figure 5.3 shows that the variation in the light collection efficiency had a negligible effect on the counting rate recorded from the system for different source positions on the plate-type detector. The normalized counting rate dropped 4 percent between source positions at 15 and 75 mm from the light pipe end. After a distance of 75 mm from the light pipe end, the variation in the normalized counting rate was not a strong function of the distance along the plate-type detector.

A full pulse height spectrum was observed for each beta source with a most-probable energy above 0.12 MeV. Pulse height spectra for beta radiation observed by the plate-type detector resemble those documented in the literature reviewed [33-34]. The observed continuous pulse height spectra indicated features corresponding to the most-probable and maximum beta energies. A Bi-210 beta energy spectrum observed by the plate-type

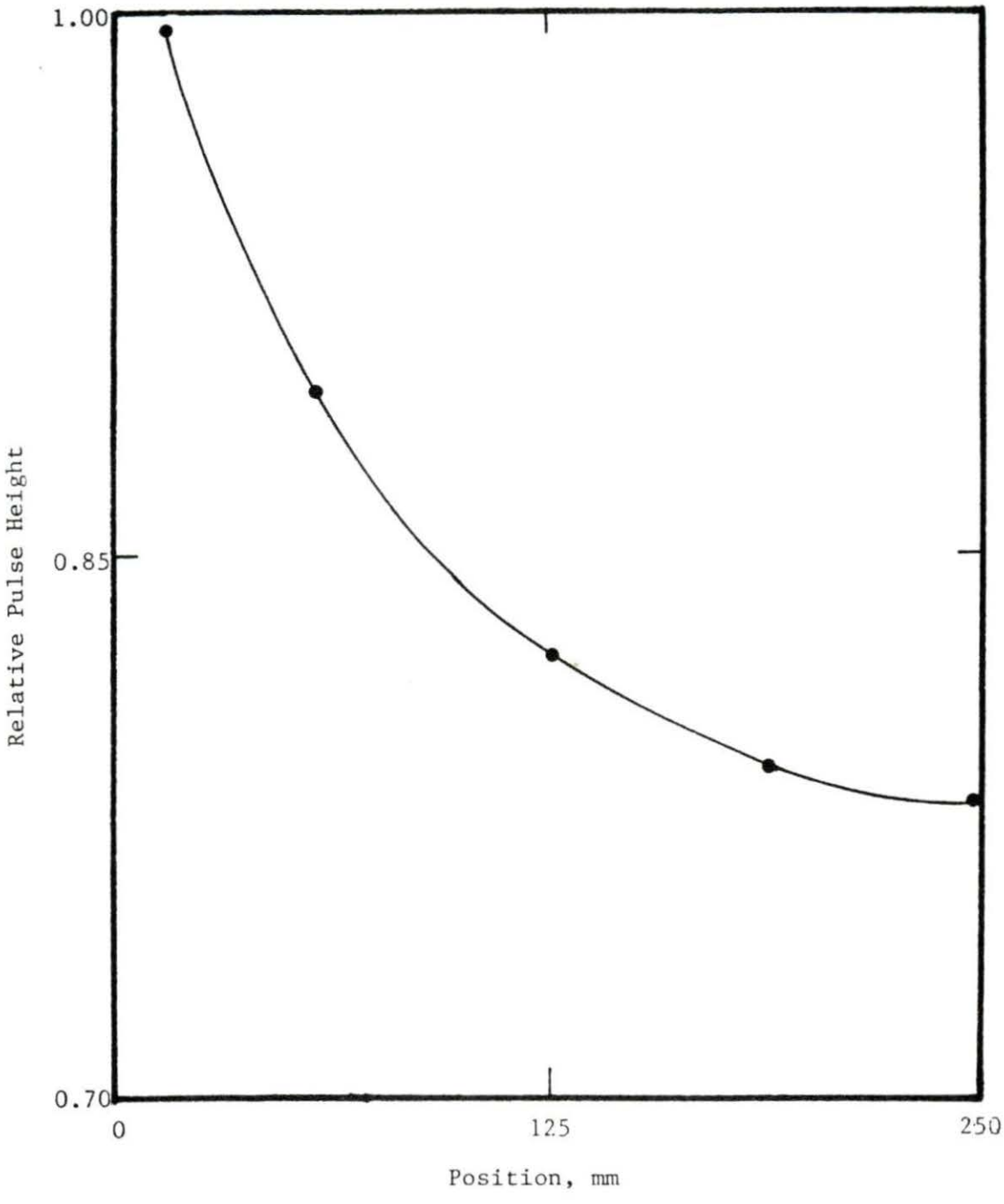

Figure 5.2. Variation of relative pulse height corresponding to the most-probable energy of a 53.4 nCi Bi-210 point source as a function of position on the centerline of the plate-type detector

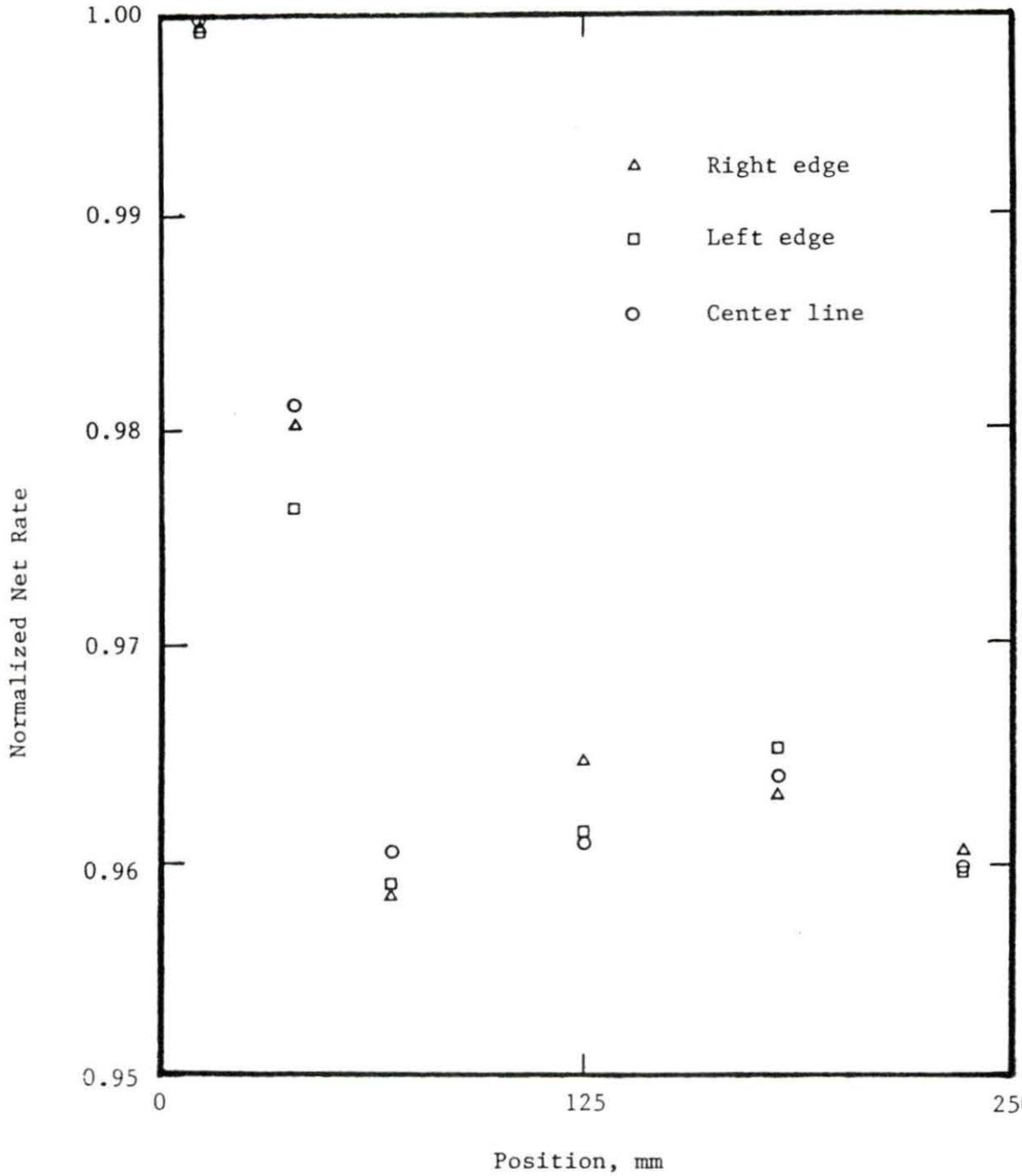

Figure 5.3. Normalized net rate from a 53.4 nCi Bi-210 beta source, E = 1.17 MeV, as a function of the source position on the detector, along the center line and 15 mm from the left edge and right edge of the plate-type detector. Net rates were normalized by the net rate 15 mm from the light pipe end along the center line

detector is shown in Figure 5.4. This spectrum displayed a most-probable beta energy at channel number 150 and a maximum beta energy at channel number 998. Due to the detection of scattered beta particles and bremsstrahlung, the lower 30 channel numbers of the spectrum displayed a tail continuum of high intensity.

Figure 5.5 displays a Tc-99 beta energy spectrum. Because its most-probable beta energy is below 0.12 MeV, the only feature visible in the beta pulse height spectrum is the maximum energy.

Figures 5.6 and 5.7 show gamma-ray spectra of Cs-137 and Co-60, respectively. These gamma-ray pulse height spectra resemble those cited in the literature reviewed [34-35]. The observed Compton distribution is distorted, resulting in a broad Compton-continuum rather than a sharp edge. The plate-type detector, in addition to all other NE 102A detectors [34-35], has very poor resolution for gamma photopeaks. In Figure 5.7, the Co-60 gamma energies were observed as a single gamma photopeak, rather than the two separate gamma photopeaks resulting with other detectors (i.e., NaI(Tl), Ge).

A beta-gamma pulse height spectrum of gaseous Ar-41 is shown in Figure 5.8. The wide continuum was caused by the variation in light collection efficiencies for the plate-type detector. The Ar-41 beta-gamma pulse height spectrum displays a wider continuum than the Bi-210 pulse height spectrum (28 keV energy difference in the maximum energy from Ar-41) shown in Figure 5.4. The continuation of the spectrum beyond channel number 1000 resulted from the detection of Ar-41 gamma-rays.

Beta energy calibration was accomplished by placing various energy-

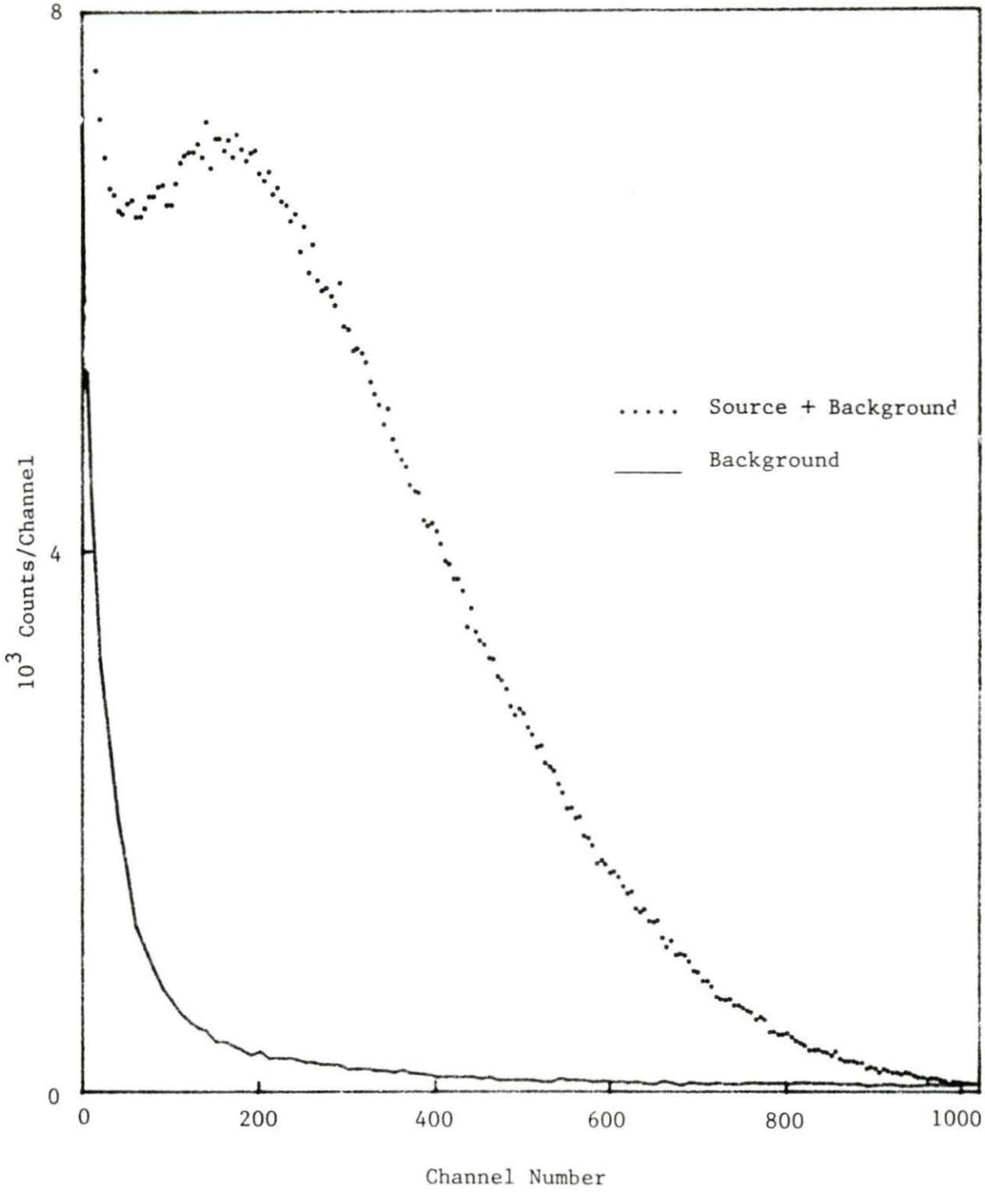

Figure 5.4. Beta pulse height spectrum for a 53.4 nCi Bi-210 (E_β(max) = 1.170 MeV) point source resting on the centroid of the 90 x 250 mm plate-type detector for a 4000 second counting time

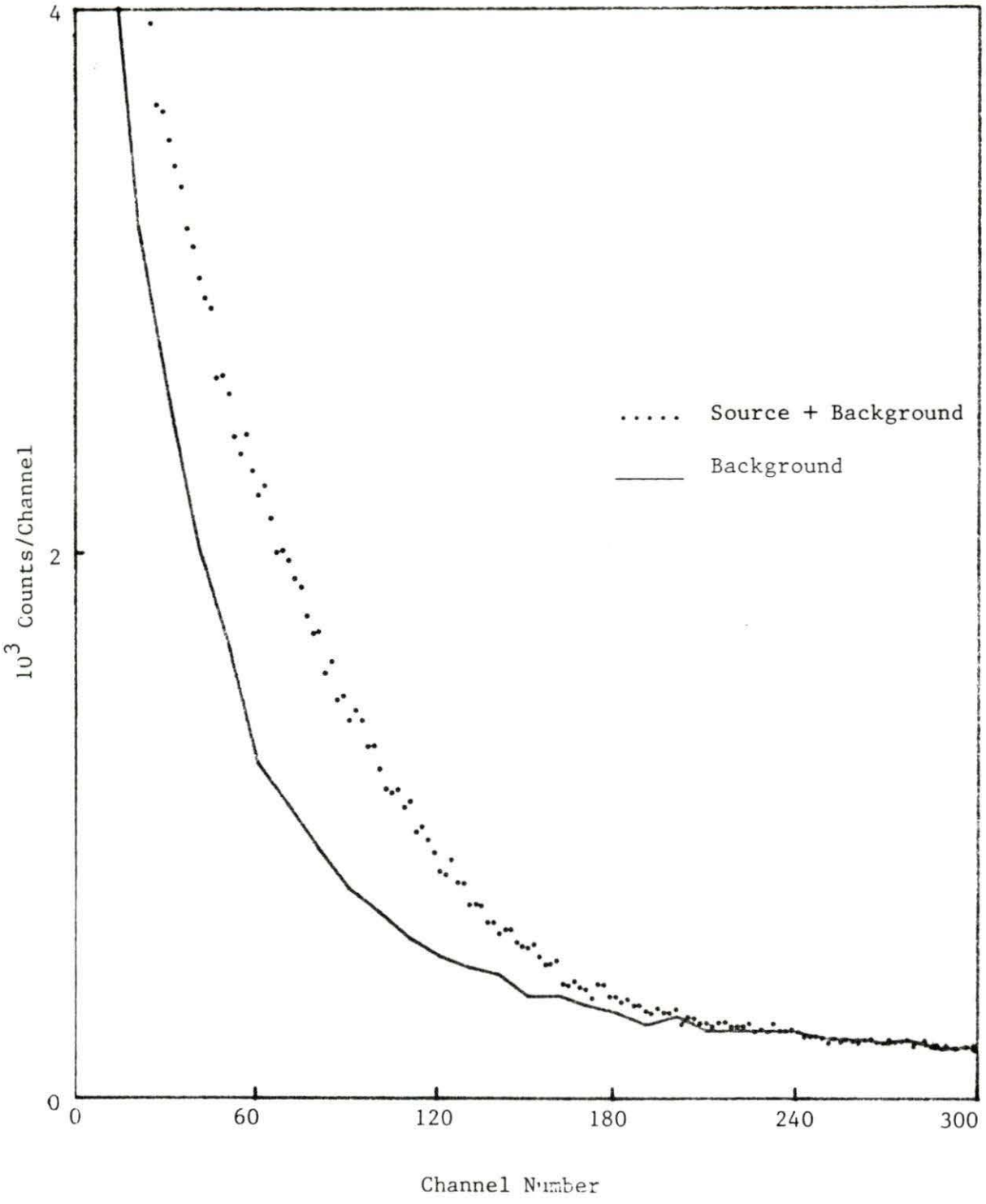

Figure 5.5. Beta pulse height spectrum for a 55.7 nCi Tc-99 (E_β(max) = 0.292 MeV) point source resting on the centroid of the 90 x 250 mm plate-type detector for a 4000 second counting time

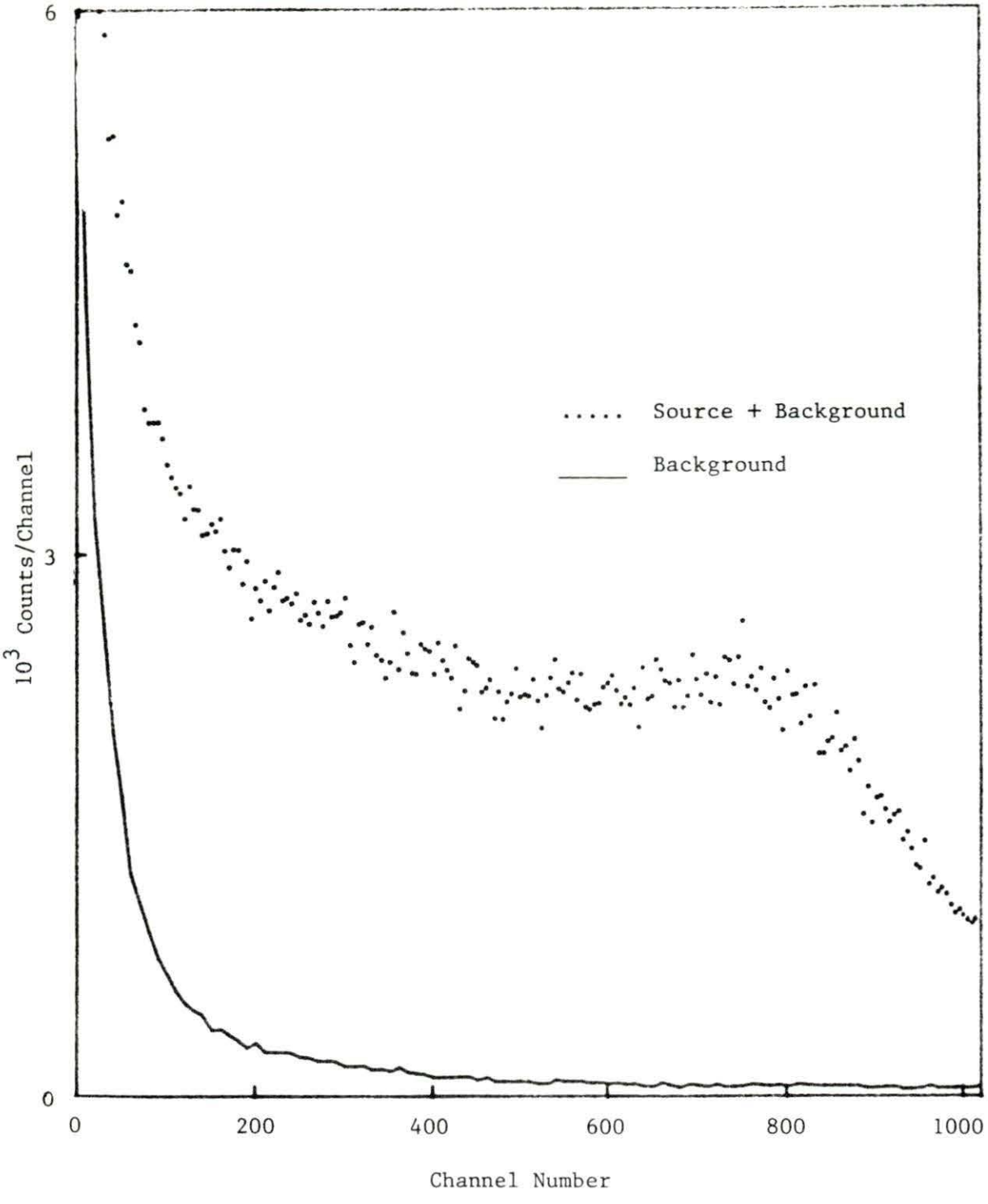

Figure 5.6. Gamma pulse height spectrum for a 200 nCi Co-60 (E_γ = 1.17, 1.33 MeV) point source resting on the centroid of the 90 x 250 mm plate-type detector for a 4000 second counting time

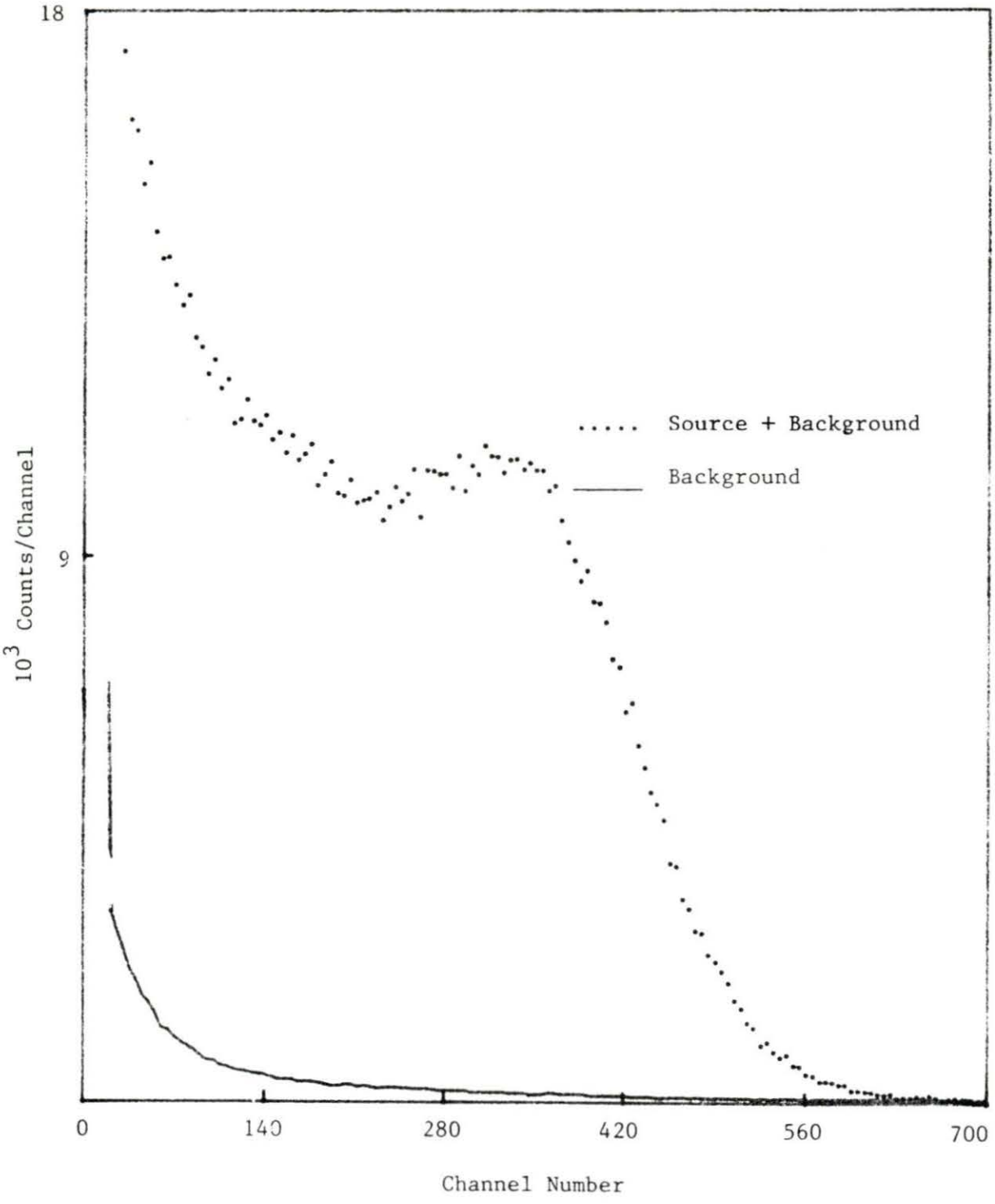

Figure 5.7. Gamma pulse height spectrum for a 830 nCi Cs-137 (E_γ = 0.662 MeV) point source resting on the centroid of the 90 x 250 mm plate-type detector for a 4000 second counting time

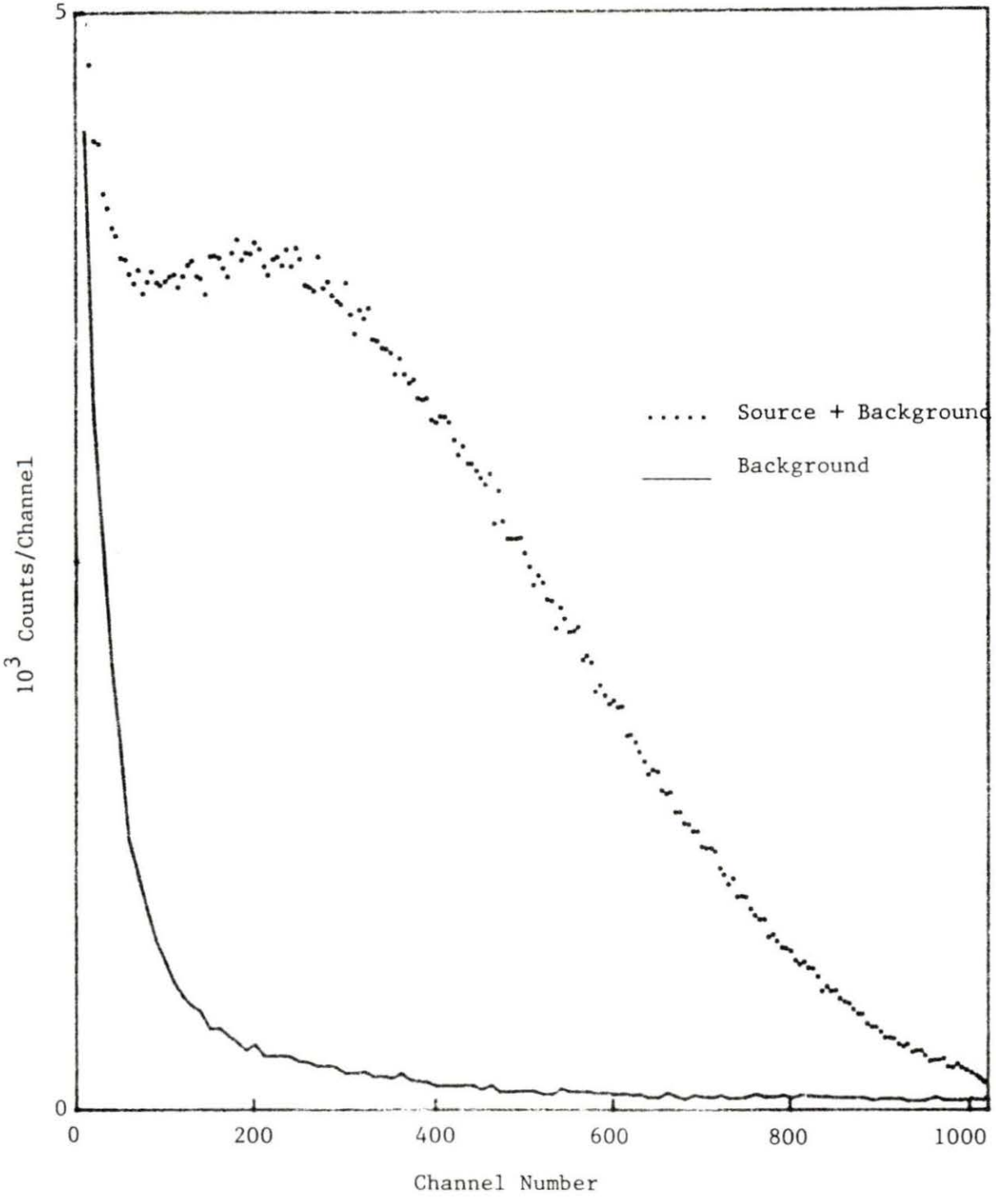

Figure 5.8. Beta-gamma spectrum for a 1.97 μCi Ar-41 (E_β(max)= 1.198 MeV, E_γ= 1.29 MeV) volume source in the plate-type detector sampling chamber for a 4000 second counting time. The continuation of the spectrum past channel 1000 resulted from the detection of Ar-41 gammas

standard sources on the symmetry line of the plate-type detector, 15 mm from the light pipe edge. This particular location was chosen because measured pulse heights were largest at this position. Table 5.4 lists the results of the beta energy calibration. Most probable beta energy values were obtained from a beta pulse height spectrum with background subtracted. Subtracting the background pulse height spectrum from a beta pulse height spectrum shifts the most probable beta energy position to a lower channel number. Maximum beta energy values were obtained by superimposing a beta pulse height spectrum with background over a background pulse height spectrum. The intersection of the two spectra indicated the maximum beta energy channel position.

The response of the plate-type detector to maximum and most probable beta energies was linear, as shown in Figure 5.9. The calibration factor was 1.14 keV/channel with a correlation of 1.0. The response of NE 102A scintillators cited in the literature review were linear in the range of beta energies from 0.125 to 10 MeV [32]. Poor resolution for gamma photopeaks inhibited gamma energy calibration.

2. Sampling chamber performance

The tests previously discussed in the Apparatus and Methods section confirmed that air leakage did not occur from the sampling chamber for a pressure differential of ± 30 mm Hg. Operating the sampling chamber above a pressure differential of 30 mm Hg caused the chamber front and back plates to deflect outward approximately 3 mm. For a pressure differential of 40 mm Hg, the side plate maximum deflection was approximately 4 mm. Thus, to avoid damaging the chamber, pressure differentials were kept

Table 5.4. Beta energy calibration data for point sources resting on the plate-type detector 15 mm from the light pipe end for 4000 second counting times

	Most Probable		Maximum	
Isotope	E (MeV)[a]	Channel	E (MeV)	Channel
Bi-210	0.188	150	1.17	998
Cl-36	0.205	161	0.714	605
Tc-99	N/A	N/A	0.292	205

[a]Values from Kaplan [33].

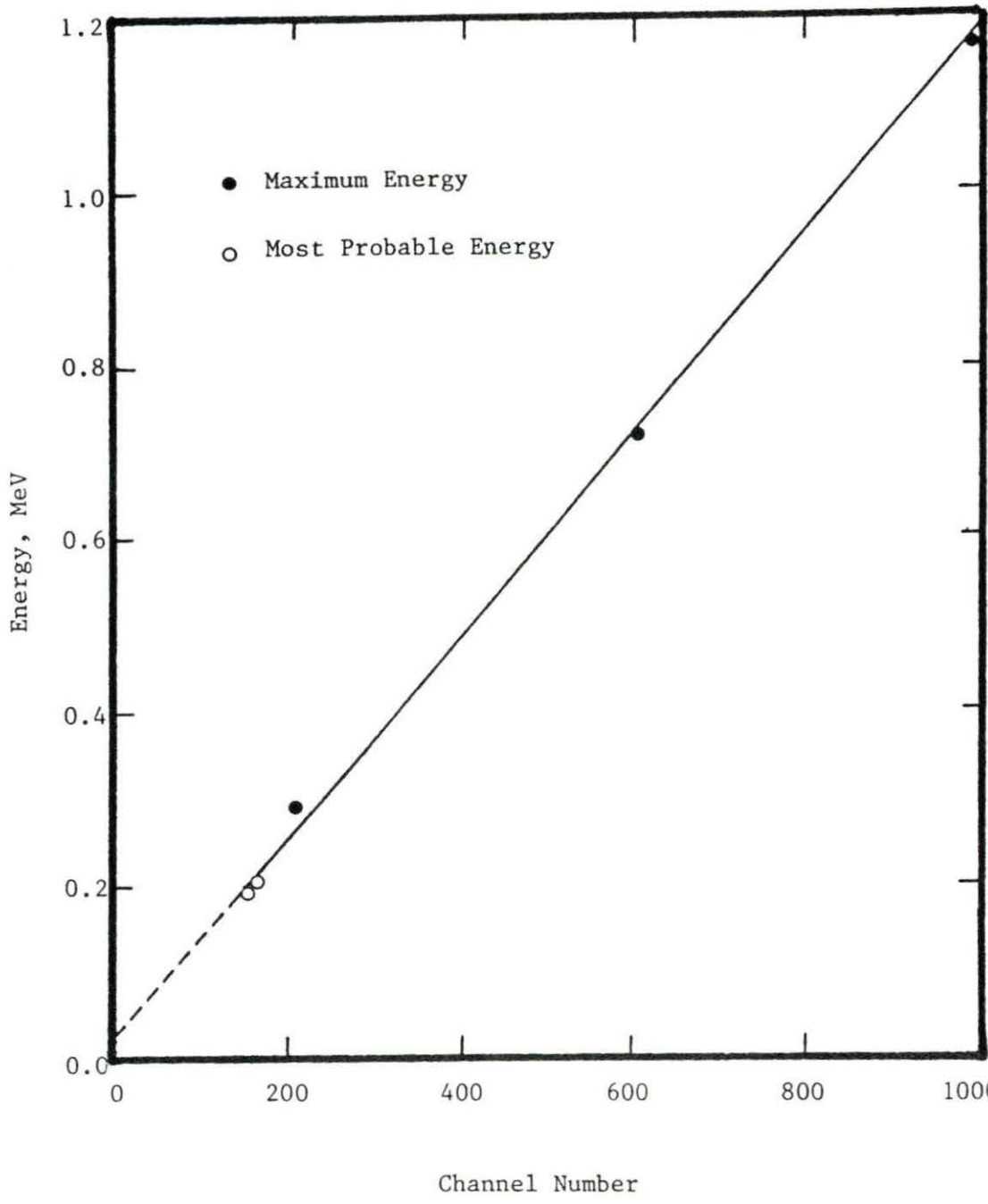

Figure 5.9. Beta energy calibration curve for most probable and maximum beta energies for the plate-type detector. The data points are from Table 5.4. The calibration factor was 1.14 keV/channel

within ± 30 mm Hg.

Homogeneous conditions existed in the sampling chamber for flow rates from 5 to 20 lpm. In this range, the smoke sample entered the sampling chamber and quickly dispersed into a thin mist visible throughout the entire chamber. For flow rates from 25 to 70 lpm, a tunneling effect occurred. The smoke did not uniformly disperse, and a steady, narrow stream was visible throughout the chamber. Therefore, flow rates were kept below 20 lpm during activity measurements to ensure homogeneous conditions in the sampling chamber.

A 90-second mixing time was observed for a 12 cc smoke sample to homogenize in the sampling chamber. This mixing time was used to ensure homogeneous conditions within the sampling chamber during Ar-41 activity calibrations.

B. Calibration of the Monitoring System

1. Argon-41 activity calibration factor

Table 5.5 displays the input data needed to determine the concentration of the argon-41 used as a calibration source in the sampling chamber. Ar-41 was the only noble gas used in the study of the response of the monitoring system because it has the greatest maximum beta energy of the noble gases of interest. This gas was manufactured locally with little expense. The Ar-41 activity was calculated by using the standard activation equation. An estimated standard error (σ_{φ}/φ) of ± 10 percent was used for the thermal neutron flux. The propagated error in the calculated Ar-41 activity was dominated by the thermal flux uncertainty. The

Table 5.5. Argon-41 calibration source activity data

Item	Value
Thermal Flux	$(1.3 \pm 0.1) \times 10^{9}$ n/cm^2-sec[a]
N_o^{40}	4.7×10^{20} atoms Ar-40
σ_a^{40}	0.65×10^{-24} cm^{-2}
$t_{1/2}^{41}$	1.83 hours
λ^{41}	0.38 hours^{-1}
Source Irradiation Time	0.5 hours
Calculated Ar-41 Source Activity	1.9 ± 0.2 μCi
System Volume	101,897 cc
Ar-41 Chamber Activity Concentration	18.6 ± 2.0 pCi/cc

[a]Standard error of ± 10 percent.

calculated Ar-41 concentration in the sampling chamber was 18.6 pCi/cc for a calculated 1.9 μCi gaseous source dispersed in a system volume of 101,897 cc.

Table 5.6 displays the output data from the calibration of the monitoring system. Three independent runs were used to determine the beta-gamma net rate obtained from the monitoring system exposed to a fixed concentration of gaseous Ar-41. The 1.83 hour half-life for Ar-41 was verified by monitoring and plotting the net rate obtained from five minute sampling times over a period of 360 minutes. The net rate was then extrapolated to the time coincident with the end of the Ar-41 and gold foil activation time. A Cs-137 gamma-ray source was counted with each activated gold foil to correct for system variations. The Cs-137 net rates were normalized by an average Cs-137 net rate obtained from all beta-gamma and gamma calibrations and were used to correct the extrapolated gold foil net rates for each individual run. The corrected gold foil net rates were then normalized by an average gold foil net rate obtained from all beta-gamma and gamma calibrations and were used to correct the extrapolated Ar-41 net rates. The three corrected net rates for Ar-41 were then averaged to give a net rate of 46854 ± 96 cpm for a beta-gamma calibration. Two independent runs were used to determine the gamma net rate with a 605 mg/cm^2 Plexiglas beta absorber encasing the plate-type detector. The same process described for beta-gamma calibration was used to give a gamma net rate of 4397 ± 30 cpm.

Background was monitored throughout the calibration process. An average of 16 five-minute sample runs, over a period of three days, was

Table 5.6. Output data from argon-41 source calibrations using the plate-type detector

Item	Value[a]
Net rate for argon-41 beta calibration	42187 ± 92 cpm
Net rate for argon-41 gamma calibration	4397 ± 30 cpm
Net rate for argon-41 beta-gamma calibration	46584 ± 96 cpm
Natural background rate	2681 ± 6 cpm
Beta-gamma detection ratio	9.59 ± 0.07
Beta detection efficiency for a 18.6 pCi/cc concentration in the sampling chamber	1.01 ± 0.11 percent
Gamma detection efficiency for a 18.6 pCi/cc concentration in the sampling chamber	0.10 ± 0.01 percent
Beta-gamma detection efficiency for a 18.6 pCi/cc concentration in the sampling chamber	1.11 ± 0.12 percent
Argon-41 beta calibration factor	$(4.4 \pm 0.4) \times 10^{-10}$ μCi/cc/cpm
Argon-41 gamma calibration factor	$(4.2 \pm 0.4) \times 10^{-9}$ μCi/cc/cpm
Argon-41 beta-gamma calibration factor	$(4.0 \pm 0.4) \times 10^{-10}$ μCi/cc/cpm

[a]The uncertainty is based on one standard deviation

used to give an average natural background rate for the monitoring system of 2681 ± 6 cpm. The beta-to-gamma detection ratio was 9.59 ± 0.11 for a gaseous Ar-41 concentration of 18.6 pCi/cc in the sampling chamber with the plate-type detector. There is a 25 percent difference between the predicted beta-gamma ratio and the measured beta-gamma ratio.

The absolute beta detection efficiency is the result of subtracting the gamma net rate from the beta-gamma net rate, and then dividing by the beta emission rate. A beta net rate of 42187 ± 92 cpm produced a beta efficiency of 1.01 ± 0.11 percent. A gamma net rate of 4397 ± 30 cpm produced a gamma efficiency of 0.10 ± 0.01 percent. The beta-gamma absolute detection efficiency is, therefore, 1.11 ± 0.12 percent. Theoretical results of the Ar-41 beta-gamma absolute detection efficiency, assuming a conversion probability of 1.0, was estimated in Theory to be 1.34 percent. The ratio between the experimental argon-41 beta-gamma absolute detection efficiency and that calculated in Theory implies an 83 percent conversion probability for argon-41 detection with the plate-type detector.

The concentration of argon-41 in the sampling chamber (18.6 pCi/cc) divided by the beta net rate (42187 ± 92 cpm) produced a beta calibration factor of $(4.4 \pm 0.4) \times 10^{-10}$ μCi/cc/cpm. The concentration of argon-41 in the sampling chamber divided by the gamma net rate (4397 ± 30 cpm) produced a gamma calibration factor of $(4.2 \pm 0.4) \times 10^{-9}$ μCi/cc/cpm. The concentration of argon-41 in the sampling chamber divided by the sum of the beta net rate and the gamma net rate resulted in a beta-gamma calibration factor of $(4.0 \pm 0.4) \times 10^{-10}$ μCi/cc/cpm.

2. Dwyer rotameter calibrations

For the range of pressure differentials and flow rates tested, the correction to the observed flow rates were less than 2 percent to obtain the true flow rates. Because the 2 percent correction for observed flow rates was within the manufacturer's stated error for the Dwyer rotameter (± 2.0 lpm), adjustments were not made for the flow rates observed during activity measurements. Table D.2 lists the true flow rates, based on the wet test meter, as a function of the Dwyer gauge reading and pressure differentials from atmospheric. Flow rates at pressure differentials other than those listed in Table D.2 may be obtained by interpolation of those given.

C. Activity Concentration Measurements

1. Monitoring system background counting rates

Table E.1 lists the component settings used and ambient conditions present during activity concentration and background measurements. Background counting rates for the unshielded sampling chamber were measured extensively before reactor operation to determine the natural background counting rate. Measurements were observed over a period of three days for counting times of 5 minutes. The natural background counting rates obtained during this three-day period are given in Table E.2. An average of the background counting rates in Table E.2 produced a natural background counting rate of 2681 ± 6 cpm. The uncertainty (± 6 cpm) was based on the square root of the sum of the total counts divided by the sum of the counting times. The Ar-41 net rate

(the critical level) that must be exceeded before a measurement is statistically different from the natural background counting rate is 13 cpm. This net rate corresponds to an Ar-41 concentration of 5.2×10^{-9} μCi/cc. The critical level at 95 percent confidence is defined by the following equation [36]:

$$L_c = 1.65 \left\{ \frac{R_b}{T_b} \right\}^{\frac{1}{2}} \left\{ 1 + \frac{T_b}{T} \right\}^{\frac{1}{2}}$$

where R_b is the background rate for a counting time of T_b minutes and T is the source plus background time. If the net rate is less than L_c, then it is not statistically different from background at the 95 percent confidence level and therefore, the sample is said to contain no measurable argon-41.

Figure 5.10 displays the gross background rates detected by both the plate-type and the NaI(Tl) detectors during reactor operation at a power level of 5 kW for one hour and after the full reactor scram. During reactor operation the unshielded plate-type detector background counting rate was approximately 8000 cpm during five-minute counting periods. The critical level for this gross background rate is 93 cpm. This net rate corresponds to a Ar-41 concentration of 3.7×10^{-8} μCi/cc. The NaI(Tl) detector, positioned in the sampling room, had a gross background counting rate of approximately 20,000 cpm during reactor operation. The NaI(Tl) detector gross background rate during reactor operation was not attributed to Ar-41. This was concluded since a photopeak corresponding to the Ar-41 gamma energy was not observed with a MCA during the one hour reactor operation.

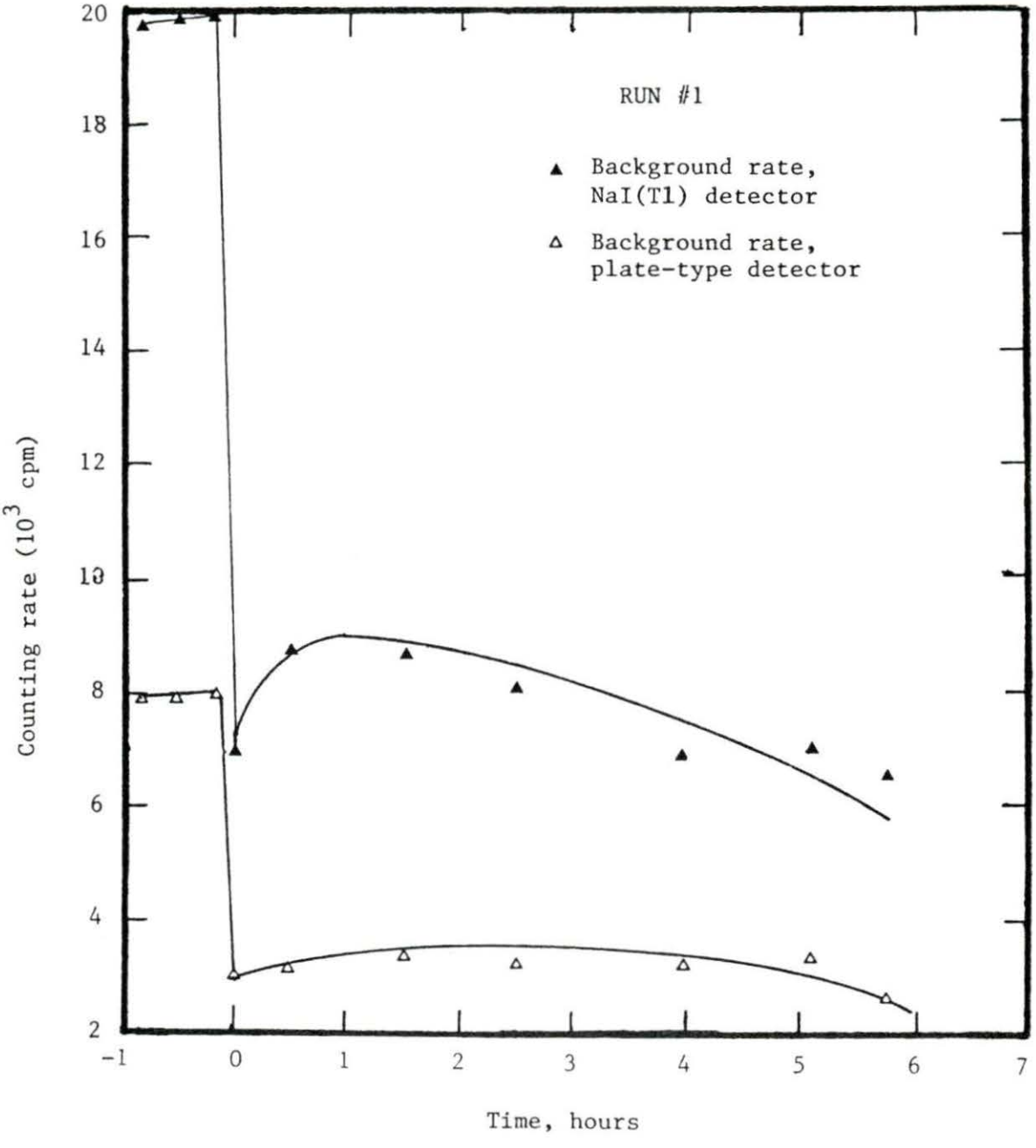

Figure 5.10. Comparison of gross background counting rates of the plate-type and the NaI(Tl) detector during reactor operation and after a reactor scram. The average ratio of background rates for the two detectors was 2.36 ± 0.20. The curves were determined by a least squares polynomial fit of degree three

After the reactor scram, the gross background counting rate detected by the unshielded plate-type detector dropped from 8000 cpm to a background counting rate near the natural background counting rate of 2681 cpm. Then, the gross background counting rate increased due to the detection of Ar-41 gamma-rays from the reactor area, even though the reactor was not operating. The gross background counting rate then reached a maximum of approximately 3300 cpm, about 600 cpm above the natural background rate, one and one-half hours after the reactor scram. The gross background counting rate gradually decayed to the natural background counting rate six hours after the reactor scram. The NaI(Tl) detector background counting rates were similar to the plate-type detector background counting rates after the reactor scram. The background counting rate above the natural background counting rate of 6700 cpm was caused by Ar-41 gamma-rays penetrating the counting room walls. The NaI(Tl) detector, operating in conjunction with a MCA, displayed a photopeak corresponding to the Ar-41 gamma-ray energy immediately after the reactor scram. When this photopeak was subtracted, the original natural background counting rate of the NaI(Tl) detector was obtained. The NaI(Tl) detector gross background counting rate dropped from 20,000 cpm to a counting rate near the natural background rate immediately after the reactor scram. The net background counting rate reached a maximum of 2000 cpm above the NaI(Tl) detector natural background counting rate one hour after the reactor scram. Six hours after the reactor scram the gross background counting rate decayed to the natural background counting rate.

A comparison of gross background counting rates from a single reactor run at 5 kW for one hour for both detectors during and after the reactor scram produced a gross background counting rate ratio of 2.36 ± 0.20. The comparison ratio was used to predict the plate-type detector monitoring system gross background counting rates from NaI(Tl) detector gross background counting rates. This enabled continuous monitoring with the plate-type detector to determine Ar-41 activity concentration levels. A second reactor run at 5 kW for one hour produced a gross background counting rate ratio of 2.40 ± 0.18.

Although the background counting rate ratios were very similar (1.7 percent difference), variations occurred in actual background counting rates between both runs. The first run, Figure 5.10, had a gross background counting rate of approximately 8000 cpm during reactor operation, 600 cpm greater than that of the second run. This difference could not be explained, since no equipment changes occurred. After the reactor scram, gross background counting rates for both runs approached the natural background counting rate for the unshielded plate-type detector (2681 cpm). After the gross background counting rate variations were determined for each run, a comparison was made between gross rates obtained during monitoring in the dynamic and static modes. Thus, Ar-41 activity concentrations could be determined for each run.

2. Argon-41 activity measurements

Figures 5.11 and 5.12 display the response of the monitoring system to releases of Ar-41 during reactor operation while monitoring two different locations. Gross counting rates and gross background counting

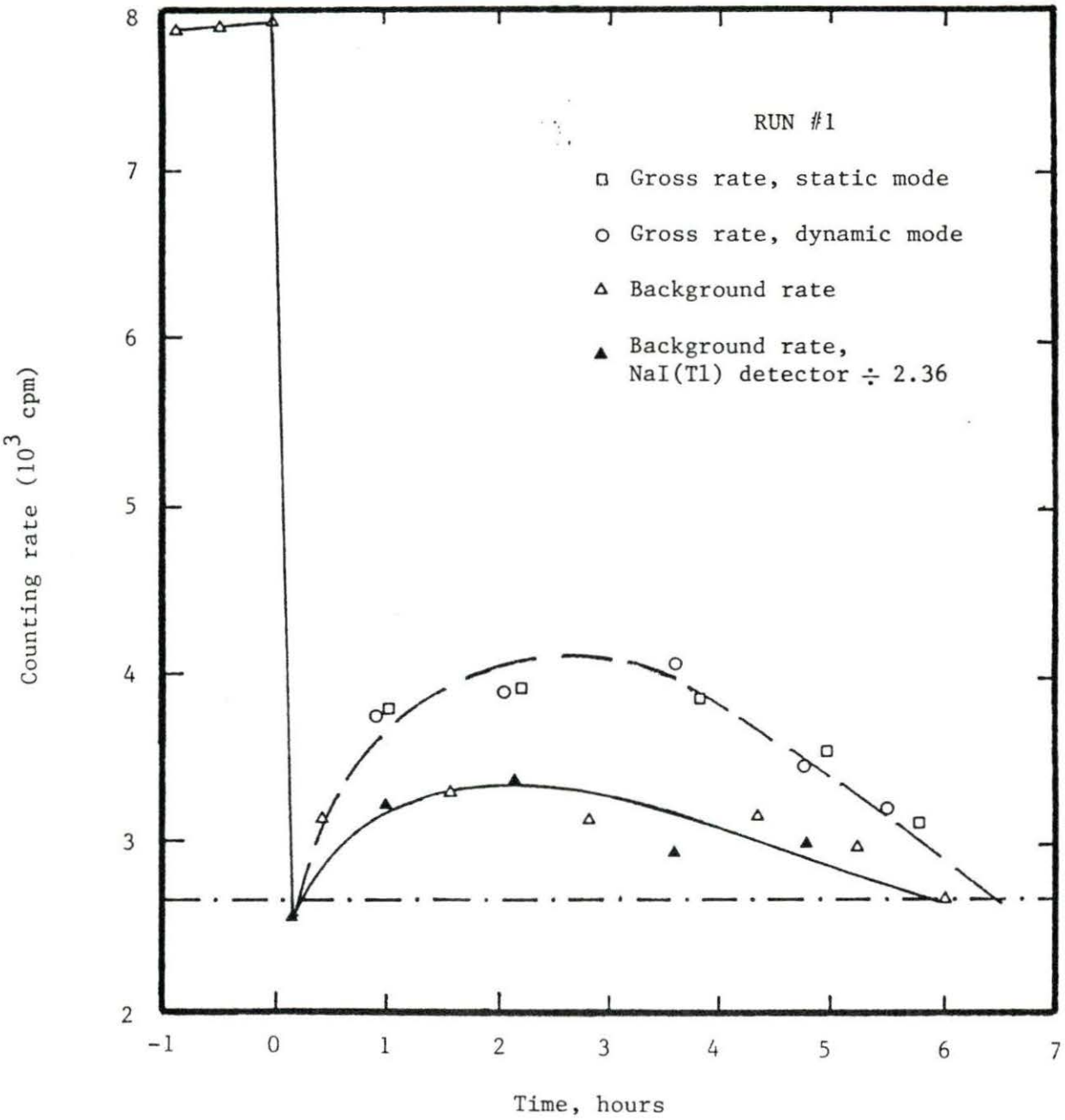

Figure 5.11. Argon-41 detection as a function of the reactor scram time (t=0). The dashed line represents the gross counting rate and the solid line represents the gross background counting rate for the unshielded monitoring system and the NaI(Tl) detector divided by 2.36. The dashed-dotted line represents the natural background detection rate (2681 cpm)

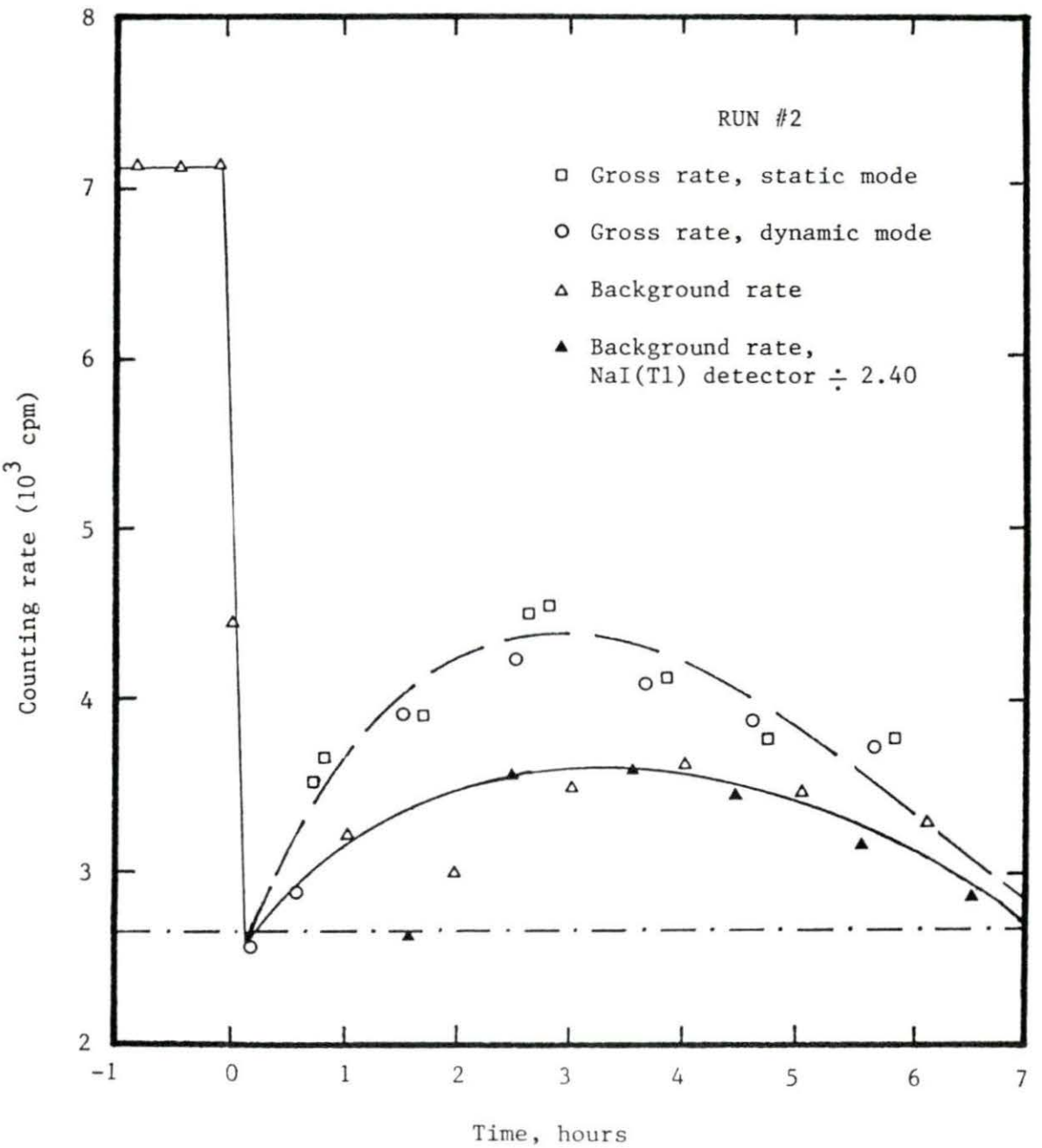

Figure 5.12. Argon-41 detection as a function of the reactor scram time (t=0). The dashed line represents the gross rate and the solid line represents the gross background rate for the monitoring system and the NaI(Tl) monitor divided by 2.40. The dashed-dotted line represents the natural background detection rate (2681 cpm)

rates were determined from five-minute sampling times. Polynomials of degree three were fitted to the gross rate and gross background rate data. Table 5.7 lists the third order polynomials determined for each run. The location of the sample line inlet during the first reactor run was 3 feet east of the reactor control panel, 4 feet above floor level. During the second reactor run, the sample line inlet was located on the second level, 10 feet south of room 215, 5 feet above floor level.

Figures 5.11 and 5.12 indicate the same general response of the unshielded plate-type detector to a release of Ar-41. While monitoring in a continuous mode, the gross counting rates reached maximum values after operating for 12 minutes at 10 lpm. The response time (12 minutes) for the dynamic case was less than the calculated transport time (15 minutes) required for an air sample to reach the chamber outlet at a flow rate of 10 lpm.

After the maximum gross counting rate was obtained, monitoring was changed to the static mode. The net counting rates for the static and dynamic cases agreed to within 3 percent after corrections were applied to compensate for decay between the sampling periods.

During both runs, a significant difference between the gross rate and the corresponding background rate became apparent after the reactor scram. At the instant of the scram, the Ar-41 activity concentration could not be measured due to large variations occurring in the background and gross counting rates. A maximum difference between the gross rate and the gross background counting rate for the first and second runs occurred 3 hours and 2½ hours after the reactor scram,

Table 5.7. Third order polynomials for the gross rate and gross background rate data plotted in Figure 5.11 and Figure 5.12. The polynomials were derived from a least squares fit

Run No.	Measurement	Third order polynomial
1	Gross rate	$20.92t^3-346.1t^2+1385.5t+2545.9$
1	Gross background rate	$16.44t^3-218.7t^2+732.2t+2609.9$
2	Gross rate	$18.52t^3-332.8t^2+1472.9t+2537.0$
2	Gross background rate	$2.703t^3-105.08t^2+619.80t+2619.1$

respectively. The maximum net rates were 871 ± 13 cpm for the first run and 875 ± 13 cpm for the second run, corresponding to maximum Ar-41 activity concentrations of (3.5 ± 0.4) x 10^{-7} μCi/cc for both runs. Tables 5.8 and 5.9 list the Ar-41 net rates, determined from the fitted functions in Figures 5.11 and 5.12, respectively, along with corresponding Ar-41 activity concentrations at half-hour intervals after the reactor scram.

Both experimental runs indicated the same maximum activity concentration. The maximum Ar-41 activity concentration from both runs was (3.5 ± 0.4) x 10^{-7} μCi/cc for a one hour reactor run at 5 kW. This activity concentration corresponds to 0.18 times the maximum permissible concentration (MPC) for a restricted personnel area and 8.4 MPC for an unrestricted personnel area, where the MPC is 2 x 10^{-6} and 4 x 10^{-8} μCi/cc for restricted and unrestricted areas, respectively [1].

The time average Ar-41 net rate is determined by subtracting the gross background rate polynomial from the gross rate polynomial (Table 5.7) and then integrating the resultant polynomial over the sampling time period (the reactor scram, zero hours, to the end of the sampling time period, six hours). For the first run, Figure 5.11, the calculated time average (over six hours) Ar-41 net rate is 609 cpm. This net rate corresponds to an Ar-41 activity concentration level of 2.4 x 10^{-7} μCi/cc. For the second run, Figure 5.12, the calculated time average (over six hours) Ar-41 net rate is 599 cpm. This net rate corresponds to an Ar-41 activity concentration level of 2.4 x 10^{-7} μCi/cc.

Integration of the Ar-41 net rate polynomials to the time when the

Table 5.8. Argon-41 net rates based on five-minute counting times with corresponding activity concentrations from run #1. The net rate was determined by subtracting the gross rate polynomial from the gross background rate polynomial in Table 5.7

Time elapsed after reactor scram (hr)	Argon-41 net rate (cpm)	Activity concentration level (μCi/cc) x 10^{-7}
0	indeterminate	indeterminate
0.5	237 ± 7	0.9 ± 0.1
1.0	466 ± 10	1.9 ± 0.2
1.5	644 ± 11	2.6 ± 0.3
2.0	769 ± 12	3.1 ± 0.3
2.5	843 ± 13	3.4 ± 0.3
3.0	871 ± 13	3.5 ± 0.4
3.5	854 ± 13	3.4 ± 0.3
4.0	798 ± 13	3.2 ± 0.3
4.5	705 ± 12	2.8 ± 0.3
5.0	578 ± 11	2.3 ± 0.2
5.5	422 ± 9	1.7 ± 0.2
6.0	239 ± 7	1.0 ± 0.1

Table 5.9. Argon-41 net rates based on five-minute counting times with corresponding activity concentrations from run #2. The net rate was determined by subtracting the gross rate polynomial from the gross background rate polynomial in Table 5.7

Time elapsed after reactor scram (hr)	Argon-41 net rate (cpm)	Activity concentration level (μCi/cc) x 10^{-7}
0	indeterminate	indeterminate
0.5	290 ± 8	1.2 ± 0.1
1.0	559 ± 11	2.2 ± 0.2
1.5	739 ± 12	3.0 ± 0.3
2.0	840 ± 13	3.4 ± 0.3
2.5	875 ± 13	3.5 ± 0.4
3.0	855 ± 13	3.4 ± 0.3
3.5	793 ± 13	3.2 ± 0.3
4.0	700 ± 12	2.8 ± 0.3
4.5	588 ± 11	2.4 ± 0.2
5.0	469 ± 10	1.9 ± 0.2
5.5	355 ± 8	1.4 ± 0.2
6.0	257 ± 7	1.0 ± 0.1

net rate became zero (when the gross rate returns to 2681 cpm, the natural background counting rate) gives the estimated time average Ar-41 net rate that is produced from a 5 kW reactor run. For the first run, the Ar-41 time average net rate (time average integration extended through 6.5 hours) for a 5 kW reactor run is 727 cpm. This corresponds to an Ar-41 activity concentration level of 2.9×10^{-7} μCi/cc. For the second run, the Ar-41 time average net rate (time average integration extended through 7.5 hours) for a 5 kW reactor run is 613 cpm. This corresponds to an Ar-41 activity concentration level of 2.5×10^{-7} μCi/cc. Table 5.10 summarizes the results of the Ar-41 activity measurements.

Table 5.11 lists estimated activity concentrations for reactor operation at various power levels and different operation times. These activity concentrations are based on measured concentrations obtained during one-hour operations from a reactor run at 5 kW. The calculated maximum Ar-41 activity concentration for an infinite-duration reactor run at 5 kW is $(1.1 \pm 0.1) \times 10^{-6}$ μCi/cc. If there is a linear relationship between argon-41 activity concentration and reactor power level, a maximum argon-41 activity concentration of $(2.2 \pm 0.2) \times 10^{-6}$ μCi/cc could be expected from an infinite-duration reactor run at 10 kW. This argon-41 activity concentration corresponds to 1.1 MPC for a restricted personnel area and 55 MPC for and unrestricted personnel area.

Table 5.10. Argon-41 activity measurements from two independent runs

Run No.	Location	Maximum activity concentration ($\mu Ci/cc$) x 10^{-7}	6-hour time average argon-41 concentration ($\mu Ci/cc$) x 10^{-7}	Time average argon-41 concentration from a 5 kW reactor run ($\mu Ci/cc$) x 10^{-7}
1	3' east of reactor control panel (EL. 4').[a]	3.5 ± 0.4[b]	2.4 ± 0.2[b]	2.9[c] ± 0.3[b]
2	10' south of Rm. 215 (EL. 5').[d]	3.5 ± 0.4[b]	2.4 ± 0.2[b]	2.5[e] ± 0.2[b]

[a] First level of nuclear reactor facility.

[b] Uncertainty is represented by one standard deviation.

[c] Average for 6.5 hours of operation.

[d] Second level of nuclear reactor facility.

[e] Average for 7.5 hours of operation.

Table 5.11. Estimated maximum argon-41 activity concentrations at different reactor powers

Reactor power (kW)	Reactor operation time	Maximum argon-41 activity concentration (μCi/cc)
5	1 hour	$(3.5 \pm 0.4) \times 10^{-7}$ [a]
5	infinite	$(1.1 \pm 0.1) \times 10^{-6}$ [b]
10	infinite	$(2.2 \pm 0.2) \times 10^{-6}$ [b]

[a] Experimental value.

[b] Calculated value.

VI. SUMMARY AND CONCLUSIONS

An unshielded noble gas monitoring system capable of measuring concentrations of argon-41 in air at 5.2×10^{-9} μCi/cc was constructed and tested. This concentration could be detected in a natural background rate of 2681 ± 6 cpm at the 95 percent confidence level. The detection of small concentration levels was achieved by sampling large volumes of air in a chamber with a large-surface-area plate-type detector. A beta-gamma sensitive plastic detector was used to identify and measure the amount of argon-41 from the continuous flow system. This technique provided the means for sampling very low concentrations with a relatively simple system.

Within the scope of the study, the following conclusions can be stated:

1. The design and construction of the monitoring system permitted operation at flow rates from 0 to 20 lpm and pressure differentials less than + 30 mm Hg.
2. Use of a wet test meter provided consistent calibration results for the Dwyer rotameter at various pressure differentials. Corrections to observed flow rates for observed pressure differentials were negligible for observed flow rates up to 20 lpm.
3. The design and construction of the plate-type detector permitted the necessary detection and identification of beta emitting isotopes. A linear energy calibration curve provided easy identification of beta emitting isotopes with maximum beta energies greater than 0.12 MeV. Gamma identification was not possible because of wide Compton-continua and poor

resolution for gamma photopeaks.

4. The 30 mg/cm^2 absorbing wrap, surrounding the 90 x 250 x 6 mm plate-type detector, was adequate for detecting beta radiation from Ar-41 and Kr-85. The current arrangement is not adequate for Xe-133 detection because the most probable beta energy is below 0.12 MeV, the attenuation energy associated with the absorber thickness.
5. The plate-type detector thickness (6 mm) was not adequate for gamma-ray detection because the absolute gamma detection efficiencies for point sources on the detector were very low.
6. The beta-to-gamma detection ratio showed that the plate-type detector was suitable for detecting argon-41 and krypton-85, since the detection ratios were very large. The current arrangement is not adequate for detecting xenon-133, because the detection ratio is less than one.
7. The detector length chosen for this study was adequate for argon-41 detection. The variation in the light collection efficiency (for various source positions on the plate-type detector) affected the signal pulse height amplitude but showed little effect on the relative counting rates. The variation in the signal pulse height amplitude affected the energy resolution. This was observed in comparing the Bi-210 (point source) and the Ar-41 (volume source) spectra. The beta continuum displayed in the argon-41 spectra was much wider than that displayed in the Bi-210 spectra, even though the energies were nearly equal.

8. The bond between the light pipe and the plate-type detector was adequate, since the variation in the relative counting rate along the light pipe edge was negligible.
9. Full pulse height spectra were observed for beta sources with a most-probable energy above 0.12 MeV. Beta sources with a most-probable energy below 0.12 MeV displayed only a tail continuum to the maximum energy. No spectra were observed for beta sources with a maximum energy below 0.12 MeV.
10. The argon-41 calibration method provided consistent calibration results. For an 18.6 pCi/cc argon-41 concentration in the sampling chamber, the argon-41 beta-gamma calibration factor is 4.0×10^{-10} μCi/cc/cpm. The detection efficiency for argon-41 is 1.11 ± 0.12 percent, a 21 percent difference from the calculated value (1.34 percent).
11. The critical level for the plate-type detector in the unshielded sampling chamber is (based on a natural background count of 214,480 detections in eighty minutes) 13 cpm. This counting rate corresponds to an argon-41 concentration of 5.2×10^{-9} μCi/cc.
12. During reactor operation, the background counting rate increased significantly and argon-41 could not be detected above the critical level during five-minute sampling times. The critical level during reactor operation was 93 cpm, corresponding to an argon-41 concentration of 3.7×10^{-8} μCi/cc.
13. Argon-41 was detected only after the reactor scram. The high

critical level during reactor operation inhibited argon-41 detection. The gross background rate was greater than the natural background counting rate after the reactor scram due to the detection of argon-41 gamma-rays from the reactor area.

14. Background counting rates from both the NaI(Tl) and the plate-type detector were similar during and after reactor runs at 5 kW. Two separate reactor runs produced similar background counting rate ratios.

15. The dynamic and static cases agreed to within 3 percent after corrections were applied for sample decay during the transport and sampling times.

16. For a 5 kW reactor run the maximum argon-41 concentration was estimated (from fitted functions to sample data) to be $(3.5 \pm 0.4) \times 10^{-7}$ μCi/cc.

17. The time average argon-41 concentration from two independent reactor runs at 5 kW was 2.4×10^{-7} μCi/cc. The calculated time average (to the time when the gross counting rate returned to the natural background rate) was 2.9×10^{-7} and 2.5×10^{-7} μCi/cc at two different locations for the first and second runs, respectively.

18. Based on a maximum argon-41 concentration of 3.5×10^{-7} μCi/cc for a one hour 5 kW reactor run, the maximum concentration from an infinite-duration 10 kW reactor run is 2.2×10^{-6} μCi/cc.

VII. SUGGESTIONS FOR FUTURE RESEARCH

The following are suggestions that might be considered by future investigators in this field.

1. The accuracy of the calibration factor may be improved by duplicating the calibration process using a calibrated argon-41 gaseous source of greater precision.
2. The source(s) of argon-41 emission may be determined by extensive monitoring with the plate-type detector system for argon-41 activity concentrations in the vicinity of the UTR-10 reactor.
3. Argon-41 activity concentration levels may be monitored during reactor operation by positioning the monitoring system in a stable background environment unaffected by reactor operation.
4. The use of the system may be extended to monitoring other radioactive noble gases, for example, Kr-85 or Xe-133, by using precision calibrated gaseous sources to repeat the measurements presented in this study.
5. The optimum detector material(s) and wrap absorption thicknesses may be determined by studying the corresponding detection efficiencies.
6. The critical level for different detector wrap absorption thicknesses may be studied by placing various beta absorbers over portions of the plate-type detector.
7. The critical level for various sampling chamber shield compositions may be studied by reducing the background rate to

obtain the necessary sensitivity for activity measurements during reactor operations.

8. The optimum detector length for argon-41 detection may be determined by using a beta shield to cover portions of the plate-type detector to observe the detection sensitivity for various detector lengths.
9. The optimum detector thickness for detection of argon-41 may be determined by studying the detector sensitivity to background radiation for various detector thicknesses.
10. The current chamber design may be improved to permit operation at increased flow rates and pressure differentials by increasing the structural strength.

VIII. REFERENCES

1. Code of Federal Regulations, Title 10, Chapter 1, Part 20 (1980).

2. C. G. Welty and M. B. Biles, Proceedings IAEA Symposium on Environmental Behavior of Radionuclides Released in the Nuclear Industry (Aix-on-Provence, France, 1973).

3. R. C. Brown, Health Physics 9, 315 (1962).

4. R. T. Graveson, IEEE Trans. Nucl. Sci. NS-22, No. 1, 654 (1975).

5. J. C. Gregory and T. A. Parnell, IEEE Trans. Nucl. Sci. NS-23, No. 1, 715 (1976).

6. J. A. B. Gibson and J. Docherty, Health Physics 28, 435 (1975).

7. H. G. Barz and W. Jacobi, Health Physics 18, 659 (1970).

8. H. G. Barz, K. D. Borchardt, and J. Hacke, Proceedings of the Seminar Monitoring of Radioactive Effluents (OECD, Paris, 1974).

9. J. D. Jones, Health Physics Operational Monitoring 2, 1043 (1972).

10. J. R. D. Stroute, Proceedings of the Seminar Monitoring of Radioactive Effluents (OECD, Paris, 1974).

11. R. A. Meck, Health Physics Operational Monitoring 2, 1029 (1972).

12. W. F. Merrit, USAEC Report No. AECL-2696 (1967).

13. E. Sakai, H. Yoshida, H. Terada, and M. Katagiri, IEEE Trans. Nucl. Sci. NS-25, No. 1, 404 (1978).

14. I. Winkelmann, IAEA Safety Series 46, 29 (1978).

15. D. W. Underhill, A. S. Goldin, and H. H. Trindade, USAEC Report NO. COO-3019-4 (1973).

16. D. S. Sasseer and C. Andreu, Proceedings of the Ninth Midyear Topical Symposium of the Health Physics Society (Rocky Mountain Chapter of the Health Physics Society, Denver, Colorado, 1976).

17. W. A. Jester and A. J. Baratta, Jr., Nucl. Technol. 56, 478 (1982).

18. R. W. Granland and D. A. Matchick, Proceedings of the Ninth Midyear Topical Symposium of the Health Physics Society (Rocky Mountain Chapter of the Health Physics Society, Denver, Colorado, 1976).

19. R. B. Hower and D. T. Rence, USAEC Report No. COO-3049-9 (1977).

20. C. W. Keil, Nucl. Safety 12, 6 (1971).

21. H. A. Bevis and B. G. Dunavent, International Journal of Applied Radiation Isotopes 16, 527 (1965).

22. USNRC, NUREG-0673 (1980).

23. C. L. Bendixsen and J. A. Buckham, USAEC Report No. CONF-730915-16 (1973).

24. F. W. Walker, G. J. Kirovac, and F. M. Rourke, Chart of the Nuclides (Knolls Atomic Power Laboratory, Schenectady, New York, 1977).

25. R. Loevinger, E. M. Japha, and G. L. Brownell, Radioisotope Sources in Radiation Dosimetry, edited by G. J. Hine (Academic Press, New York, 1956).

26. A. F. Rohach, private communication, May 1983.

27. J. R. Lamarsh, Introduction to Nuclear Engineering (Addison-Wesley, Reading, Massachusetts, 1977).

28. R. P. Benedict, Fundamentals of Temperature, Pressure and Flow Measurements, (John Wiley & Sons, New York, 1977).

29. J. Klinsky, private communication, April 1983.

30. ASTM, private communication, April 1983.

31. R. L. Heath, Scintillation Spectrometry, Gamma-Ray Spectrum Catalog, Second Edition, Vol. 1, IDO-16880-1 (1964).

32. G. F. Knoll, Radiation Detection and Measurement (John Wiley & Sons, New York, 1979).

33. I. Kaplan, Nuclear Physics (Addison-Wesley, Reading, Massachusetts, 1963).

34. F. H. Wohn, J. R. Clifford, G. H. Carlson, and W. L. Talbert, Jr., Nuclear Instruments and Methods 101, 343 (1972).

35. E. Nardi, Nuclear Instruments and Methods 95, 229 (1971).

36. L. A. Currie, Analytical Chemistry 40, 586 (1968).

IX. ACKNOWLEDGEMENTS

The author expresses a great deal of thanks to his major professor, Dr. R. A. Hendrickson. Without his knowledge of the subject, insight into the problem, and gentle nudging, this study would not have come into being. Anyone who has completed graduate work knows how inadequate these few words are.

The financial support and technical services supplied by the Affiliate Research Program in Electrical Power was extremely instrumental in the progress of this study. The Environmental Health and Safety staff and the Nuclear Engineering Department reactor technician, Elden Plettner, have my appreciation for services rendered. Dr. A. F. Rohach also has my appreciation for help received in developing computer programs used in this research. In addition, the author is very grateful to his uncle, Mr. William Gilbert, for inspiring the author to enter the nuclear engineering curriculum. The author wishes to thank his parents, Robert and Barbara Montgomery, for their encouragement and support over the years. Finally, the author thanks his wife, Rosemary Ann, for her help and understanding through the years of study.

X. APPENDIX A: POINT DETECTOR IN A CYLINDRICAL CHAMBER

```
C     THIS PROGRAM CALCULATES THE BETA INCIDENCE RATE FOR A
C     POINT DETECTOR IN A SEMI-INFINITE CYLINDRICAL CHAMBER
C     OF VARYING RADIUS.
      DIMENSION S(300)
C     S                 INCIDENCE RATE ARRAY
      DO 30 J=1,100
      RADIUS=J*10
C     RADIUS            RADIUS OF SEMI-INFINITE CYLINDER(CM)
      ANTAIR=12.9
C     ANTAIR            BETA MASS ABSORPTION COEFFICIENT(CM**2/GM)
C                       IN AIR WITH E(MAX)=1.198 MEV
      AIRDN=1.205E-03
C     AIRDN             DENSITY OF AIR(730MMHG AND 293K)
C     INTEGRATION OVER 1.57 RADIANS(π/2)
C     X                 INTEGRATION ANGLE IN RADIANS
      DO 10 I=1,157
      X=I*0.01
      B=RADIUS/(COS(X))
      EQUATION FOR INCIDENCE RATE CALCULATION
      S(I)=((COS(X))**2)*(1-EXP(-ANTAIR*AIRDN*B))
   10 CONTINUE
C     TRAPIZOID NUMERICAL INTEGRATION IN STEPS
C     OF 0.01 RADIANS
      DO 20 I=1,157
      Z=Z*0.5*0.01*(S(I)+S(I+1))
   20 CONTINUE
C     PRINT RADIUS(CM) OF CYLINDER AND CORRESPONDING
C     INCIDENCE RATE(BETAS/SECOND) FOR RADII FROM 10
C     TO 1000 CM IN INCREMENTS OF 10 CM, 1000 CM IS
C     THE MAXIMUM RANGE IN AIR FOR BETA PARTICLES
C     WITH MAXIMUM ENERGY 1.198 MEV
      Z=Z/4./ANTAIR/AIRDN
      PRINT*,'RADIUS = ' ,RADIUS,'INCIDENCE RATE = ',Z
   30 CONTINUE
      STOP
      END
```

XI. APPENDIX B: POINT DETECTOR IN A RECTANGULAR PRISM

```
 1:C     THIS PROGRAM CALCULATES THE BETA OR GAMMA INCIDENCE
 2:C     RATE FOR A PLANE DETECTOR IN A RECTANGULAR PRISM.
 3:C     THE PROGRAM IS AUTOMATICALLY SET UP TO CALCULATE THE
 4:C     BETA INCIDENCE RATE FOR A QUARTER SECTION OF A 90 X
 5:C     250 MM PLANE DETECTOR IN THE BASE PLANE OF A
 6:C     RECTANGULAR PRISM USING A 1/4 CM POINT DETECTOR MESH
 7:C     WITH A 1 CM CHAMBER WALL MESH.  THE PRINTED
 8:C     RESULT IS THE INCIDENCE RATE (#/SEC)
 9:C     FOR A UNIT/CM**3/SEC SOURCE.
10:C     DEFINITION OF PROGRAM PARAMETERS:
11:C     XMU             ATTENUATION COEFFICIENT IN AIR(1/CM)
12:C                     BETA=0.016,GAMMA=6.97E-05.
13:C     X1,X2,Y1,Y2     SUMMATION LIMITS IN THE X AND Y
14:C                     DIRECTIONS.  DEFINES THE DISTANCE
15:C                     FROM THE POINT DETECTOR(ORIGIN)
16:C                     TO THE PRISM WALLS.
17:C     Z               SUMMATION LIMIT IN THE Z
18:C                     DIRECTION.  DEFINES THE PERPENDICULAR
19:C                     DISTANCE FROM THE CHAMBER WALL TO
20:C                     THE DETECTOR PLANE
21:C     NX,NY,NZ        DEFINES THE NUMBER OF PRISM WALL
22:C                     INTERVALS IN THE  X, Y, AND Z DIRECTIONS,
23:C                     THESE ARE THE AREAS IN WHICH CONES
24:C                     ARE GENERATED ON THE PRISM WALLS.
25:C     ONE OUTPUT LINE IS PRINTED,  THIS IS
26:C     THE INCIDENCE RATE FOR A 90 X 250 MM
27:C     PLANE DETECTOR IN A 40 X 63 X 20 CM PRISM.
28:      XMU=0.016
29:      Z=20.
30:      NX=40.
31:      NY=63.
32:      NZ=20.
33:      DO 40 I=1,49,2
34:      STEP1=I/4.
35:      Y1=-31.5-STEP1
36:      Y2=31.5-STEP1
37:      DO 40 J=1,17,2
38:      STEP2=J/4.
39:      X1=-20-STEP2
40:      X2=20-STEP2
41:      DX=(X2-X1)/NX
42:      DY=(Y2-Y1)/NY
43:      DZ=(Z/NZ)
44:      Y1S=Y1**2
45:      Y2S=Y2**2
46:      DXDZ=DX*DZ
```

```
47:       X=X1-DX/2.
48:C      SUMMATION IN Y DIRECTIONS
49:       DO 10 N=1,NX
50:       X=X+DX
51:       XS=X**2
52:       XY1S=XS+Y1S
53:       XY2S=XS+Y2S
54:       Z=-DZ/2.
55:       DO 10 M=1,NZ
56:       Z=Z+DZ
57:       ZS=Z**2
58:       RS1=XY1S+ZS
59:       RS2=XY2S+ZS
60:       SINP1=Y1/SQRT(XY1S)
61:       SINP2=Y2/SQRT(XY2S)
62:       SINT1=SQRT(XY1S/RS1)
63:       SINT2=SQRT(XY2S/RS2)
64:       DEL=-SINP1*SINT1*DXDZ/RS1
65:       SUM=SUM+DEL
66:       R=SQRT(RS1)
67:       COST=Z/R
68:       SUMM=SUMM+(1.-EXP(-XMU*R))*COST*DEL
69:       DEL=SINP2*SINT2*DXDZ/RS2
70:       SUM=SUM+DEL
71:       R=SQRT(RS2)
72:       COST=Z/R
73:       SUMM=SUMM+(1.-EXP(-XMU*R))*COST*DEL
74: 10    CONTINUE
75:C
76:       X1S=X1**2
77:       X2S=X2**2
78:       DYDZ=DY*DZ
79:       Y=Y1-DY/2
81:C      SUMMATION IN X DIRECTIONS
82:       DO 11 N=1,NY
83:       Y=Y+DY
84:       YS=Y**2
85:       YX1S=YS+X1S
86:       YX2S=YS+X2S
87:       Z=-DZ/2.
88:       DO 11 M=1,NZ
89:       Z=Z+DZ
90:       ZS=Z**2
91:       RS1=YX1S+ZS
92:       RS2=YX2S+ZS
93:       SINP1=X1/SQRT(YX1S)
94:       SINP2=X2/SQRT(YX2S)
95:       SINT1=SQRT(YX1S/RS1)
96:       SINT2=SQRT(YX2S/RS2)
```

```
 97:       DEL=-SINP1*SINT1*DYDZ/RS1
 98:       SUM=SUM+DEL
 99:       R=SQRT(RS1)
100:       COST=Z/R
101:       SUMM=SUMM+(1.-EXP(-XMU*R))*COST*DEL
102:       DEL=SINP2*SINT2*DYDZ/RS2
103:       SUM=SUM+DEL
104:       R=SQRT(RS2)
105:       COST=Z/R
106:       SUMM=SUMM+(1.-EXP(-XMU*R))*COST*DEL
107: 11    CONTINUE
108:C
109:       ZS=Z**2
110:       DXDY=DX*DY
111:       Y=Y1-DY/2.
112:C      SUMMATION IN Z DIRECTION
113:       DO 12 N=1,NY
114:       Y=Y+DY
115:       YS=Y**2
116:       X=X1-DX/2.
117:       DO 12 M=1,NX
118:       X=X+DX
119:       XS=X**2
120:       RS=XS+YS+ZS
121:       R=SQRT(RS)
122:       COST=Z/R
123:       DEL=COST*DXDY/RS
123:       SUM=SUM+DEL
124:       SUMM=SUMM+(1.-EXP(-XMU*R))*COST*DEL
125: 12    CONTINUE
126:C
127:       SUMM=SUMM/4./3.14159/XMU
128:       SUMMM=SUMMM+SUMM
129:       SUM=0
130:       SUMM=0
131: 40    CONTINUE
132:       PRINT*,SUMMM
133:       STOP
134:       END
```

XII. APPENDIX C: PROCEDURES FOR PREPARING THE WET TEST METER

Before flow calibrarion began, the WTM was flushed and tested to ensure the manufacturer's specified accuracy of ± 0.5 percent. To prepare the WTM, it was necessary to drain all fluids and remove any debris that would restrain its proper operation. First, the meter was drained by removing the bottom and top port plugs. A high pressure air stream (30 psig) was inserted in the top port to blow any debris out through the bottom port. The meter was then filled with distilled water and allowed to operate for 15 minutes. This loosened or dissolved any debris left in the meter. Again, the meter was drained and blown out with a high pressure line. The meter was filled once more and was then ready for a leak test.

The procedure used to check for leaks in the WTM was similar to that for the sampling chamber. While the meter valves were closed, the meter pressure was maintained at -15 mm Hg below atmospheric, the manufacturer's limit, for 10 minutes, demonstrating that no water or air leakage was occurring.

The next step was to level the meter by means of the adjusting screws in the feet and by reference to the spirit level on the meter. Operating the meter for about two hours was necessary to saturate the meter fluid with air. Once completed, the water calibration level was adjusted for the 0.1 cubic foot per revolution for the WTM dial. The water level was adjusted by opening both inlet and outlet WTM connection valves. The water level in the meter was adjusted until the point of the marker inside the gauge glass (right side of the meter

chamber) coincided with its reflection in the under-surface of the water meniscus. If the WTM operated correctly, no further adjustments were necessary. Correct operation was verified by comparing results obtained to that from another calibrated flow measurement device, e.g., the Dwyer rotameter used in this study.

XIII. APPENDIX D: CORRECTIONS TO WTM FLOW RATES

The gas volume noted on the meter upon completion of a calibration test was measured at saturation and ambient pressure and temperature. For complete accuracy, corrections were made for the dry gas at a standard temperature and pressure. From Boyles' and Charles' laws, the equation for the standard flow rate is

$$Q_s=(T_s/T_o)(P_o/P_s)Q_o$$

where

T_s= standard temperature (K),

P_s= standard pressure (mm Hg),

Q_o= meter reading divided by time interval (lpm),

T_o= meter temperature (K),

P_o= meter pressure from absolute minus vapor pressure of meter liquid (mm Hg).

The correction factor for the gas volume is

$$F = (288.72/T_g)(P_t-P_{svp}/748.746),$$

where

T_g= gas temperature (K),

P_t= total gas pressure (mm Hg),

P_{svp}= saturated vapor pressure of meter fluid at temperature T_g (mm Hg).

Table D.1 displays the results of three different flow rate correction methods: standard pressure and temperature with

Table D.1. WTM flow rates corrected to various pressures and temperatures

Dwyer Gauge Reading (lpm)	STP[a]+GCF[b] (lpm)	SPRT[c]+GCF[b] (lpm)	SPRT[c] (lpm)
5	4.19	4.74	5.01
10	8.44	9.44	10.01
15	12.54	14.26	14.96
20	16.68	18.16	19.95
25	21.63	24.40	24.98
30	26.03	29.47	29.93

[a]Standard temperature (273.15 K) and pressure (760 mm Hg).

[b]Gas correction factor.

[c]Standard pressure (760 mm Hg) and room temperature (293.15 K).

the gas correction factor, standard pressure and room temperature with the gas correction factor, and standard pressure and room temperature without the gas correction factor. All Dwyer flow rates during argon-41 activity concentration measurements were corrected to standard pressure and room temperature, because of good agreement with the wet test meter flow rates. Table D.2 lists the true flow rate (WTM), corrected to standard pressure and room temperature, as a function of the Dwyer gauge reading and pressure differentials from atmospheric.

Table D.2. True flow rates[a] (lpm) as a function of the Dwyer gauge reading (WTM) and pressure differentials from atmospheric

ΔP (mm Hg) \ Dwyer Gauge Reading (lpm)	5	10	15	20	25	30
0	5.01	10.01	14.96	19.95	24.98	29.93
-5	5.00	9.98	14.95	19.91	24.89	29.87
-10	4.97	9.93	14.91	19.87	24.83	29.80
-20	4.93	9.87	14.83	19.74	24.67	29.61
-30	4.90	9.80	14.76	19.63	24.53	29.48

[a]Corrected to standard pressure (760 mm Hg) and room temperature (293.15 K).

XIV. APPENDIX E: SUPPORTING TABLES

Table E.1. Component settings and atmospheric conditions present during argon-41 activity measurements

Item	Value
Amplifier gain	186
Bias voltage	+900 volts
Flow rate	10.0 lpm
Ambient temperature[a]	22.4 °C
Atmospheric pressure[a]	732.6 mm Hg
Relative humidity[a]	79 %
Pressure drop[a]: Tubing inlet to chamber outlet	+4.80 mm Hg
Ambient temperature[b]	24.5 °C
Atmospheric pressure[b]	725.1 mm Hg
Relative humidity[b]	82 %
Pressure drop[b]: Tubing inlet to chamber outlet	+4.85 mm Hg

[a] First run.

[b] Second run.

Table E.2. Natural background counting rates based on five-minute sample times for the plate-type detector positioned in the unshielded sampling chamber

Number	Background counting rate (cpm)
1	2715[a]
2	2660[a]
3	2638[a]
4	2650[a]
5	2689[b]
6	2693[b]
7	2714[b]
8	2634[b]
9	2753[b]
10	2671[b]
11	2685[c]
12	2684[c]
13	2717[c]
14	2676[c]
15	2674[c]
16	2643[c]

[a]First measurement period.

[b]Second measurement period.

[c]Third measurement period.